

Rigorous Analysis of Reversible Faradaic Depolarization Processes in the Electrokinetics of the Metal/Electrolyte Solution Interface

J. F. L. Duval* and H. P. van Leeuwen

Department of Physical Chemistry and Colloid Science, Wageningen University, Dreijenplein 6, 6703 HB Wageningen, The Netherlands

J. Cecilia

Departament de Matemàtica, Universitat de Lleida, Rovira Roure 177, 25198 Lleida, Spain

J. Galceran

Departament de Química, ETSEA, Universitat de Lleida, Rovira Roure 177, 25198 Lleida, Spain

Received: February 28, 2003; In Final Form: May 6, 2003

The bipolar faradaic depolarization of the interface metal/solution is examined for the situation in which the transversal electron transfer is limited by mass transfer of the components of a reversible redox couple. Transversal diffusion of the electroactive species to and from the surface and lateral convective mass transport, resulting from a pressure gradient applied along the surface, are taken into account. The analysis first focuses on the case in which the lateral electric field required for bipolar behavior is externally applied through the solution. Numerical analysis of the intrinsic nonlinear coupling between the convective-diffusion equation and the Poisson equation for finite currents allows derivation of the spatial distribution of the potential and the concentration profiles of the electroactive species. The corresponding distribution of the local faradaic current density along the metallic surface and the ensuing overall bipolar current are obtained. Characteristics of the conductivity curves, bipolar current versus applied field, are given for different sets of electric and hydrodynamic parameters. Then, on the basis of these results, the analysis of bipolar faradaic depolarization process is extended to electrokinetic phenomena, in particular streaming potential.

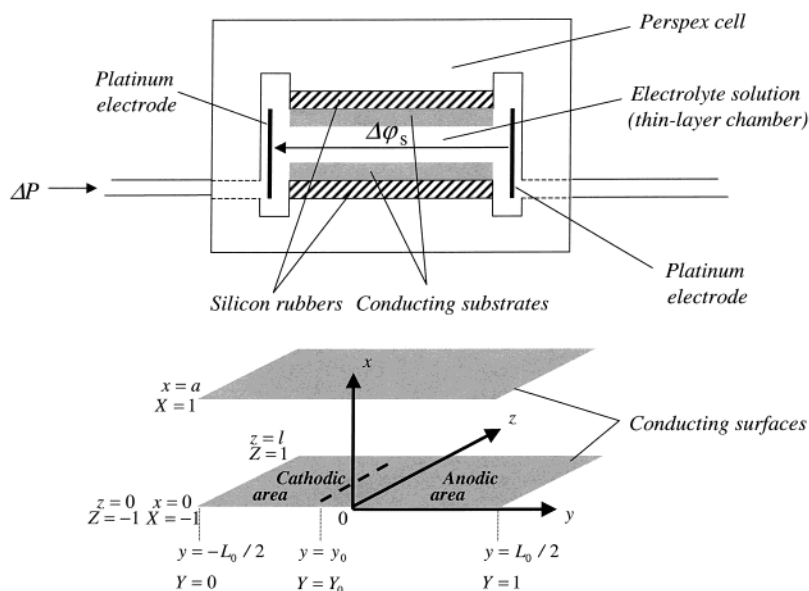
1. Introduction

Electrokinetic phenomena are characterized by tangential motion of liquid with respect to an adjacent charged surface. In electrophoresis, the relative motion between fluid and charged particles is caused by an externally applied electric field.^{1,2} In streaming potential experiments, displacement of the mobile part of the diffuse charge, induced by a lateral applied pressure gradient, generates a potential difference across the cell, the streaming potential.³ These are examples of so-called electrokinetic phenomena of the first kind. The relationship between the driving force (electric field and pressure) and the resulting measured quantity (velocity and streaming potential, respectively) is linear and at low driving force described by the classical Helmholtz–Smoluchowski (H–S) equation,^{4–5} valid for $\kappa a_p \gg 1$, κ being the reciprocal Debye length and a_p the particle radius. Theoretical expressions applicable to the case $\kappa a_p \ll 1$ also point out linearity.^{6,7} Regardless of the complications brought about by possible surface conduction,⁸ use of the H–S equation leads to a straightforward estimation of the electrokinetic potential.⁹

In electrokinetic phenomena of the second kind,¹⁰ the linearity between the applied driving force and the measured electrokinetic quantity is lost. For instance, in very strong electric fields (10^2 – 10^3 V cm⁻¹), the electrophoretic velocities of metallic particles in aqueous electrolyte are reported to be 1 or 2 orders of magnitude *higher* than those predicted by the H–S equation.¹¹ On the other hand, streaming potentials for metals in the

presence of electroactive (i.e., redox active) electrolyte are *lower* than the ones expected on the basis of the classical linear H–S equation.¹²

The common basis for the “superfast” electrophoresis and the collapse of streaming potential for conducting materials is the occurrence of *bipolar faradaic depolarization*. When metallic particles dispersed in an aqueous medium are subjected to sufficiently strong electric fields, the spatial distribution of the potential difference between metal and solution allows bipolar electrolysis of water: at one side of the particle, water reduction generates an anionic cloud, and at the other, water oxidation yields a cationic cloud. As a result, different ionic concentration polarization zones (space charge regions) are electrochemically generated at the two sides of the particle. An additional process that may contribute to the formation of these space charge regions is the behavior of the counterions of the double layer under condition of high applied fields. As observed by means of preliminary Monte Carlo simulations (Lyklema, De Coninck, unpublished results), these ions have the tendency at high electric fields to leave the surface and its vicinity. The modification of the local field due to the induced space charges results in superfast electroosmosis and electrophoresis. Streaming potentials generated by metallic surfaces in electroactive electrolyte are diminished because of the extensive electronic conduction inherent with the bipolar electrolysis process taking place at the metal surface. If these faradaic processes are carried by an electrochemically reversible redox couple, even low streaming



Typical dimensions of the cell: $L_0 = 7.6\text{cm}$ $l = 2.6\text{cm}$ $a = 0.20\text{mm}$

Figure 1. Schematic representation of the thin flat-layer cell. Notations.

potentials (or low pressure gradients) suffice to induce significant bipolar depolarization.

To our knowledge, rigorous analysis of bipolar faradaic depolarization processes interfering with the electrokinetics of the metal/solution interface has not been tackled yet. Baran et al.¹¹ give a theoretical expression for the velocity of metallic particles in strong electric fields on the basis of the velocity estimated for ion exchanger particles, which may show superfaster electrophoresis.¹³ The analysis provided¹¹ basically relies on the assumption of a linear distribution for the potential tangential to the particle surface. The electrophoretic velocity, v_{ef} , is then obtained after replacing the ζ -potential in the classical H-S equation by the local potential drop across the region where the space charge exists. The result is of the form

$$v_{\text{ef}} \propto (2E_0 a_p - \Delta\phi^d)^2 (2\gamma - 1) \quad (1)$$

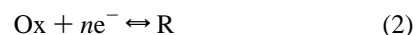
where E_0 is the undisturbed externally applied field, $\Delta\phi^d$ is the overpotential required for water electrolysis, and γ is a coefficient characterizing the fraction of the total potential drop that occurs on either side of the particle. Though eq 1 is reported to satisfactorily explain experimental data, it is based on the approximation of a linear potential distribution around the particle, which is inconsistent with the magnitude of the overall bipolar faradaic current for the typical range of fields applied through the particle. As demonstrated for bipolar planar surfaces^{12,14} and bipolar spherical particles,^{15,16} there is an intrinsic *nonlinear* coupling between the distribution of the current at the particle surface and the spatial course of the electric field. The more significant the electronic bipolar conduction as compared to the bulk solution conduction is, the more the potential distribution deviates from linearity. Besides, no analysis of the mass transport (coupled convective diffusion and conduction) of the induced space charges is explicitly mentioned in ref 11, and no connection is made with the bipolar electrochemical behavior of dispersions of spherical metallic particles.^{17,18} A quantitative understanding of the electrokinetic properties of the metal/electrolyte solution interface under conditions leading to phenomena of the second kind necessarily

requires a more advanced investigation of the corresponding bipolar faradaic processes.

In this paper, we propose a theoretical analysis for faradaic depolarization processes occurring at metallic surfaces in an electroactive electrolyte solution. Mass transport of the electroactive species, including transversal diffusion to and from the surface and lateral convection due to the tangential pressure gradient, is considered for the typical streaming potential conditions in which the lateral field is coupled to the applied pressure gradient. Estimation of the substrate bipolar conductance term for given lateral field and mass-transfer conditions allows (i) a quantitative interpretation of the experimentally observed nonlinear relationship between streaming potential and applied pressure gradient and (ii) an estimation of the ζ -potential of the metal/electroactive solution interface. Corresponding interpretation of experimental data for gold in the presence of the $\text{Fe}(\text{CN})_6^{3-}/\text{Fe}(\text{CN})_6^{4-}$ redox couple illustrates the applicability of the streaming potential technique for probing double-layer properties of metals in the presence of reversible redox systems.¹⁹

2. Mass-Transfer Limited Bipolar Faradaic Process Induced by an Externally Applied Electric Field

2.1. Description of the Problem. Let us consider two parallel planar conducting surfaces placed in a thin-layer cell as depicted in Figure 1. The distance between the two metallic electrodes in the flat capillary cell is a , the length of the metallic surface L_0 and its width l . The electrolyte solution of bulk conductivity K^L , relative dielectric permittivity ϵ_r , and (dynamic) viscosity η contains a redox couple denoted as Ox/R that exhibits electrochemically reversible behavior for the particular conducting substrates considered. This means that no appreciable activation barrier is observed for the electron-transfer reaction at the metallic surfaces



where n is the number of electrons, e^- , involved. A potential difference, $\Delta\phi_{\text{ss}}$, is applied to the solution in the thin-layer cell

across its long side. As shown in Figure 1, the cell is connected to two reservoirs containing the electrolyte solution.²⁰ A pressure gradient, ΔP , is applied, which forces the solution to flow from left to right through the thin-layer chamber between the two surfaces. For convenience, the Cartesian coordinate system (x, y, z) is defined such that the origin coincides with the position halfway the conducting surface placed at the bottom of the cell. In a previous analysis,¹² we demonstrated that, because of the absence of activation energy for the electron-transfer reactions (eq 2), anodic and cathodic electrochemical reactions concomitantly occur at the extremities of the two surfaces as soon as a finite $\Delta\phi_s$ is effective. The two surfaces behave as bipolar electrodes. We arbitrarily locate the *positive* side of the field applied in the left part of the thin-layer chamber, where consequently the *cathodic* reaction takes place. In the following, it will be convenient to use the dimensionless spatial variables X, Y, Z defined as

$$X = \frac{2}{a} \left(x - \frac{a}{2} \right) \quad Y = \frac{1}{L_0} \left(y + \frac{L_0}{2} \right) \quad Z = \frac{2}{l} \left(z - \frac{l}{2} \right) \quad (3)$$

The solution is supposed to contain an excess of supporting electrolyte so that conductive transport of the electroactive compounds is not taken into account. Electron transfer (eq 2) is then rate-limited by the diffusion to and from the surfaces of the electroactive species Ox and R and by the convective flow due to the imposed ΔP . To derive the overall bipolar current, denoted I_t , analysis of the hydrodynamic situation is first required. Then, the set of equations for the calculation of the concentration profile of Ox/R, the spatial distributions of the potential, and the local faradaic current density along the surfaces can be formulated.

2.2. Velocity Profile. The direction of the bulk stream of flow is parallel to the surfaces (y -direction), and the steady-state velocity profile is represented by $v_Y(X, Z)$, as formulated by the pertaining Navier–Stokes equation,

$$\frac{\partial^2 v_Y(X, Z)}{\partial X^2} + \phi^2 \frac{\partial^2 v_Y(X, Z)}{\partial Z^2} = - \frac{a^2 \Delta P}{4\eta L_0} \quad (4)$$

with $\phi = a/l$. For the pressure domain considered in this paper, the steady-state assumption is always valid because the time τ_C required for the fluid to pass the distance L_0 ($\tau_C = L_0/v_0$) is typically 1 or 2 orders of magnitude lower than the measurement time τ_M of streaming potential ($\tau_M \approx 20$ – 30 s). At the walls of the parallelepipedic cell, we have the boundary conditions

$$v_Y(X=\pm 1, Z) = v_Y(X, Z=\pm 1) = 0 \quad (5)$$

Considering the typical range of applied pressures, the flow is assumed laminar as in agreement with $Re < 2500$, where Re is the Reynolds number. The general solution, $v_Y(X, Z)$, of eqs 4 and 5 is written²¹

$$v_Y(X, Z) = v^0 \left\{ (1 - X^2) + \frac{32}{\pi^3} \sum_{m=1}^{\infty} \frac{(-1)^m}{(2m-1)^3} \times \right. \\ \left. \cos \left[(2m-1) \frac{\pi X}{2} \right] \cosh \left[(2m-1) \frac{\pi Z}{2\phi} \right] \operatorname{sech} \left[(2m-1) \frac{\pi l}{2\phi} \right] \right\} \quad (6)$$

where v^0 is the characteristic velocity given by

$$v^0 = \frac{a^2 \Delta P}{8\eta L_0} \quad (7)$$

The first term within brackets in eq 6 represents the classical parabolic Poiseuille profile. The second term accounts for the contribution of the walls positioned at $Z = \pm 1$ (edge effects). As expected, the magnitude of this latter contribution is correlated to the geometrical factor ϕ . For intermediate to high ϕ , the summation term in eq 6 cannot be neglected with respect to the parabolic profile term, whereas for low ϕ , it is negligible. At a given Y , the velocity indeed virtually remains constant over most of the range of Z values: only within a short distance from the walls at $Z = \pm 1$, the velocity drops to zero. For the type of thin-layer cell discussed here (Figure 1), ϕ is not more than 0.01. Hence, in the following, we shall only consider the Poiseuille profile for an infinitely wide channel ($\phi \rightarrow 0$).

2.3. Coupling between the Convective-Diffusion Equation and the Poisson Equation. The concentration profiles of the electroactive species, denoted as $c_{Ox}(X, Y)$ and $c_R(X, Y)$ for the Ox and R species, respectively, are determined by the field and the characteristics of the diffusive and convective mass-transport processes. Symmetry of the problem with respect to the Z -dimension follows from the previous discussion and justifies that c_{Ox} and c_R are not functions of Z . Considering that typically $L_0 \gg a$ and $l \gg a$ ($\phi \ll 1$), the concentration polarization of Ox and R in the Y - and the Z -directions may also be neglected. Transient effects will not be considered here, which is in agreement with $\tau_D = (\delta^2/(\pi D)) \ll \tau_M$, τ_D being the typical time required for building-up a diffusion layer of thickness δ and D being the diffusion coefficient. Consequently, the local faradaic currents along the surfaces are limited by diffusion of the species in the X -direction and by convection in the Y -direction. By way of example, we examine the cathodic reaction and the profile for $c_{Ox}(X, Y)$. We define the dimensionless concentration difference with respect to the bulk,

$$C_{Ox}(X, Y) = \frac{c_{Ox}(X, Y) - c_{Ox}^*}{c_{Ox}^*} \quad (8)$$

where c_{Ox}^* is the bulk concentration of species Ox, that is, the initial homogeneous concentration of Ox. Under the conditions outlined above and with the velocity profile as derived in the previous section, the Nernst–Planck equation reduces to the convective-diffusion equation,

$$v^0(1 - X^2) \frac{\partial C_{Ox}(X, Y)}{\partial Y} = \frac{4D_{Ox}L_0}{a^2} \frac{\partial^2 C_{Ox}(X, Y)}{\partial X^2} \quad (9)$$

where D_{Ox} is the diffusion coefficient of Ox. Resolution of eq 9 requires two boundary conditions with respect to X and one related to the Y -direction. This latter is simply written

$$C_{Ox}(X, Y=0) = 0 \quad (10)$$

which expresses that, at the left side of the channel, electroactive species are injected from the reservoir with bulk concentrations c_{Ox}^* and c_R^* . The remaining conditions derive from the coupling of the equations expressing the mass balances for Ox and R and the reversible property of the redox couple. If we assume equal diffusion coefficients ($D_{Ox} = D_R = D$),

$$C_{Ox}(X=\pm 1, Y) = \frac{c_{Ox}^* + c_R^*}{c_{Ox}^*} f_{Ox}(Y) - 1 \quad (11)$$

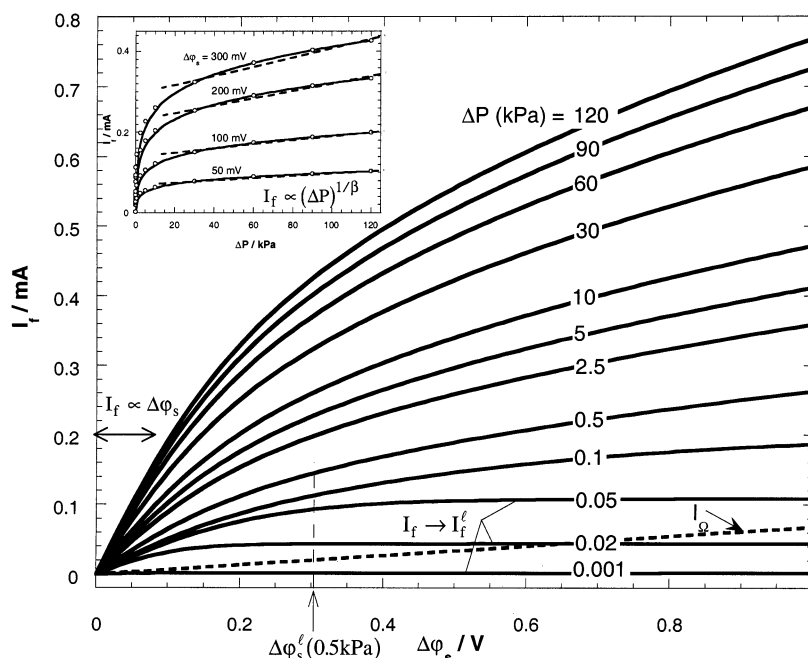


Figure 2. Bipolar current as a function of the applied lateral field (conductivity curves) at different ΔP (indicated in kPa). The ohmic current I_Ω is mentioned for comparison purposes. Model parameters are as follows: $a = 0.2$ mm; $L_0 = 7.6$ cm; $l = 2.6$ cm; $D = 10^{-9}$ m² s⁻¹; $V^0 = -233$ mV; $K^L = 1$ Ω⁻¹ m⁻¹; $c_{Ox}^* = c_R^* = 0.1$ mM. In the inset, I_f is set against ΔP for various $\Delta\phi_s$ (points). The results are fitted with an expression of the form $(\Delta P)^{1/\beta}$ with $\beta \approx 5$ (solid curves). The dashed curves in the inset represent linear fits for high ΔP (see section 2.4.2).

which is complementary to the profile $C_R(X, Y)$. f_{Ox} is a function defined by the Nernst-type relationship

$$f_{Ox}(Y) = \frac{\exp[-nf(V(Y) - V^0)]}{1 + \exp[-nf(V(Y) - V^0)]} \quad (12)$$

$V(Y)$ is the potential of the solution at the position Y with respect to the (equipotential) metallic surfaces, V^0 is minus the standard potential of the redox couple Ox/R, and f is the constant

$$f = \frac{F}{RT} \quad (13)$$

F being the Faraday constant, R the gas constant, and T the absolute temperature. Relation 12 expresses the equilibrium between the concentrations of the redox species at the surface and the potential $V(Y)$. For further detail, the reader is referred to ref 14.

To find the profiles of Ox, the spatial course of the potential $V(Y)$ must be known. There is an intrinsic nonlinear coupling between $C_{Ox}(X, Y)$ and $V(Y)$, as subsumed in eqs 11–12. The equation defining $V(Y)$ is provided by the electroneutrality condition written for every X – Z slice along the surfaces. In the geometry considered here, the resulting Poisson equation for finite currents is written

$$\frac{aK^L}{L_0^2} \frac{d^2 V(Y)}{dY^2} + 2j(Y) = 0 \quad (14)$$

where $j(Y)$ is the local faradaic current density at the position Y defined by

$$j(Y) = \frac{2nFDc_{Ox}^*}{a} \left[\frac{\partial C_{Ox}(X, Y)}{\partial X} \right]_{X=+1} = - \frac{2nFDc_{Ox}^*}{a} \left[\frac{\partial C_{Ox}(X, Y)}{\partial X} \right]_{X=-1} \quad (15)$$

The derivation of eq 14 is given in detail in ref 14. Here, we shall only recall the approximations made and the conditions for which these are valid: that is, (i) the potential distribution related to the double-layer formation at the two interfaces metal/solution is neglected, which is justified provided that the Debye length, κ^{-1} , is much smaller than the position-dependent diffusion layer thickness, $\delta(Y)$, and the gap a between the two parallel surfaces; (ii) the electric field across the solution is assumed to be time-independent, and the hydrodynamic and the diffusion processes have reached steady-state conditions; (iii) the chemical composition of the solution remains essentially constant during the experiment (constant K^L), which is the case for indifferent ions in sufficient excess over the electroactive species (this also ensures the validity of $\kappa^{-1} \ll \delta(Y)$). The two boundary conditions related to eq 14 are provided by the potential balance in solution and the condition of no-charge accumulation in the conducting substrates¹⁴

$$V(Y=0) - V(Y=1) = \Delta\phi_s \quad (16)$$

$$\left. \frac{dV(Y)}{dY} \right|_{Y=0} = \left. \frac{dV(Y)}{dY} \right|_{Y=1} \quad (17)$$

Determination of $C_{Ox}(X, Y)$, $j(Y)$, and $V(Y)$ requires numerical resolution of the system of coupled eqs 9–12 and 14–17. Details of the computational procedure are reported in the Appendix. Once $j(Y)$ is known for given $\Delta\phi_s$ and ΔP , the corresponding overall bipolar current I_f is obtained by integration of the local current density $j(Y)$ ^{12,14,22}

$$I_f = -2lL_0 \int_{Y_0}^{Y_0} j(Y) dY = 2lL_0 \int_{Y_0}^1 j(Y) dY \quad (18)$$

where Y_0 is the position for which $j(Y=Y_0) = 0$. The corresponding potential difference between solution and metallic phase, $V(Y=Y_0)$, corresponds to the local equilibrium potential, V^* . If eqs 14 and 18 are combined, I_f may also be expressed as

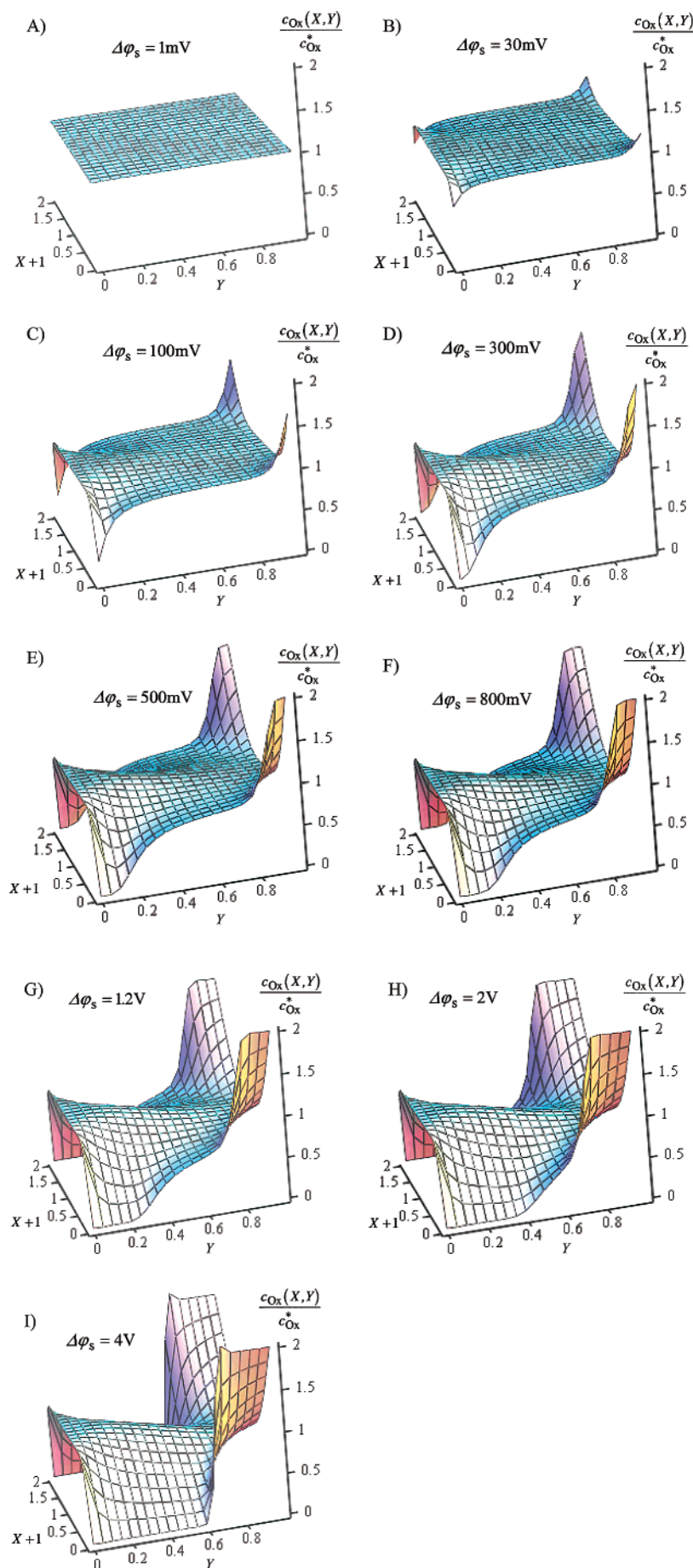


Figure 3. Concentration profiles of the oxidized form of the redox couple at varied applied fields $\Delta\phi_s$ (indicated) and at the pressure $\Delta P = 0.5$ kPa (section 2.4.1). Model parameters are as follows: $a = 0.2$ mm; $L_0 = 7.6$ cm; $l = 2.6$ cm; $D = 10^{-9}$ m² s⁻¹; $V^0 = -233$ mV; $K^L = 1$ Ω⁻¹ m⁻¹; $c_{Ox}^* = c_R^* = 0.1$ mM. The profiles at the injection position $Y = 0$ (left extremity of the cell) are not drawn ($c_{Ox} = c_{Ox}^*$).

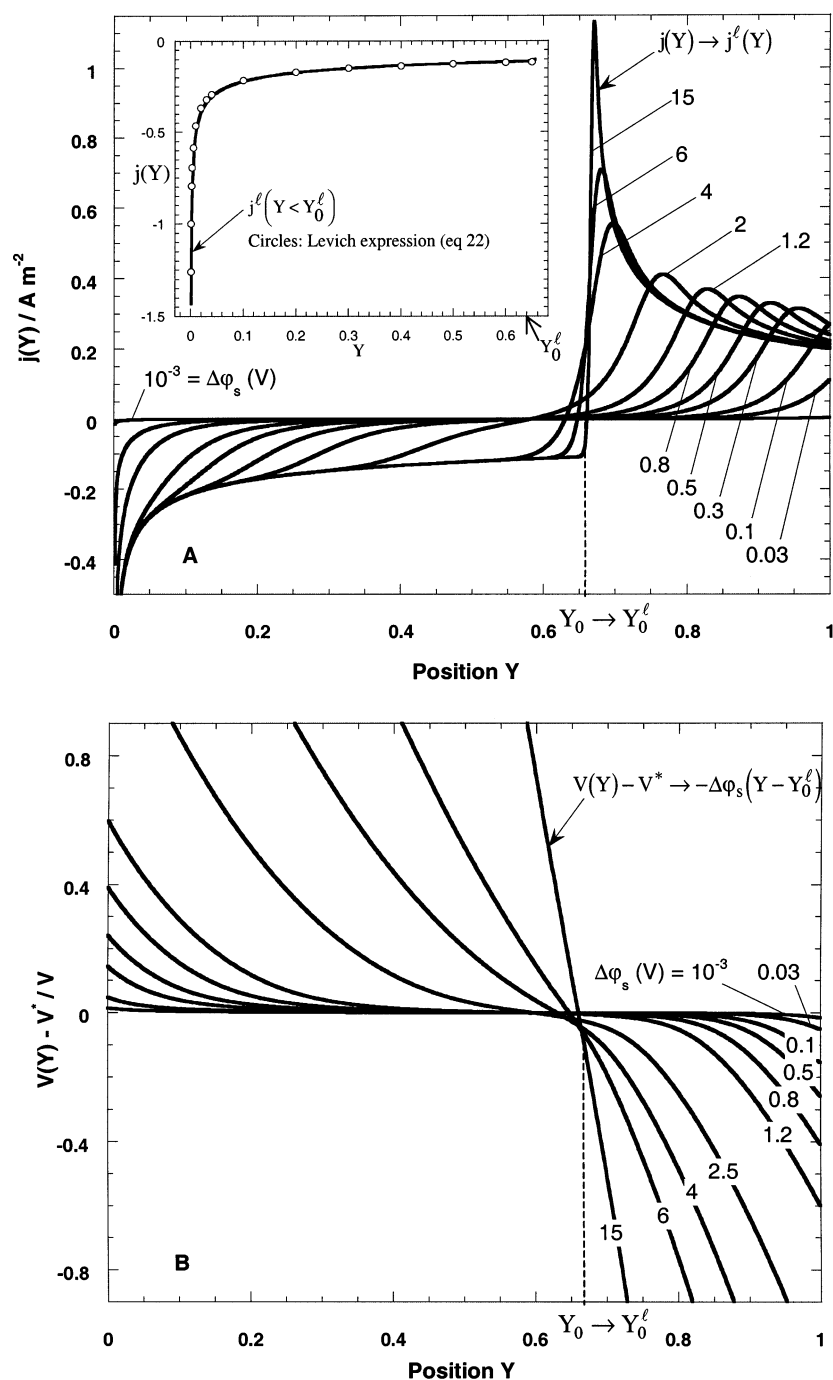


Figure 4. Spatial distributions of (A) the local faradaic current density $j(Y)$ and (B) the local potential $V(Y)$ along the conducting surface at different applied fields $\Delta\phi_s$ (indicated) and at the pressure $\Delta P = 0.5$ kPa. In the inset of panel A, the limiting current $j^\ell(Y)$ pertaining to the cathodic area is plotted and compared to the current density calculated with eq 22. Model parameters are as follows: $a = 0.2$ mm; $L_0 = 7.6$ cm; $l = 2.6$ cm; $D = 10^{-9}$ m² s⁻¹; $V^0 = -233$ mV; $K^L = 1$ Ω⁻¹ m⁻¹; $c_{Ox}^* = c_R^* = 0.1$ mM.

a function of the electric field at the position $Y = Y_0$ compared to the front or back edge of the cell ($Y = 0$ or $Y = 1$),

$$I_f = \frac{aK^L}{L_0} \left(\left. \frac{dV(Y)}{dY} \right|_{Y=Y_0} - \left. \frac{dV(Y)}{dY} \right|_{Y=0} \right) = \frac{aK^L}{L_0} \left(\left. \frac{dV(Y)}{dY} \right|_{Y=Y_0} - \left. \frac{dV(Y)}{dY} \right|_{Y=1} \right) \quad (19)$$

2.4. Results and Discussion. Typical plots of the bipolar current I_f as a function of the lateral field $\Delta\phi_s$ are shown in Figure 2 for different values of the applied pressure ΔP . For

low to intermediate $\Delta\phi_s$, I_f increases steeply before leveling off. For low ΔP (≤ 50 Pa), I_f asymptotically approaches a constant value with increasing $\Delta\phi_s$. For larger ΔP , this limit is reached for larger fields ($\Delta\phi_s > 1$ V, not shown). These characteristic features of the conductivity curves can be interpreted after examination of the concentration profiles upon variation of the hydrodynamic and electric parameters.

2.4.1. Analysis at Given Pressure Gradient, ΔP , and Different Lateral Fields, $\Delta\phi_s$. The profiles $c_{Ox}(X, Y)$ are given in Figure 3 for $\Delta P = 0.5$ kPa and various $\Delta\phi_s$. The corresponding spatial distributions of the current density $j(Y)$ and of the potential $V(Y)$ are given in Figure 4. At $\Delta\phi_s = 0$, the potential drop $V(Y)$ at

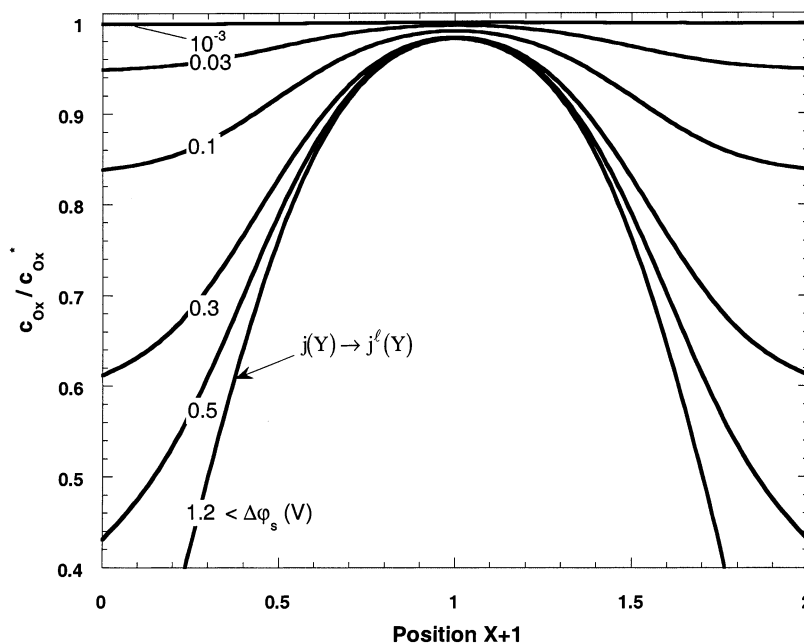


Figure 5. Cross sections of the concentration profiles $c_{\text{Ox}}/c_{\text{Ox}}^*$ represented in Figure 3 at the position $Y = 0.221$ providing an illustration of the depletion of the electroactive compounds upon increase of $\Delta\varphi_s$ (indicated in V). For the position Y chosen, the diffusion-limited flux is reached for $\Delta\varphi_s \geq 1.2$ V.

the interface metal/solution is, for every position Y along the surface, the Nernst potential, V^N , as defined by

$$V^N = V^0 - \frac{1}{nf} \ln \left(\frac{c_{\text{Ox}}^*}{c_{\text{R}}^*} \right) \quad (20)$$

In this case, the local surface concentrations equal their bulk values (Figure 3A), and consequently, $j(Y)$ and I_f are zero. As soon as $\Delta\varphi_s$ is finite, bipolar conduction takes place in accordance with the slope $dI_f/d(\Delta\varphi_s)$ at $\Delta\varphi_s = 0$ (which is finite for a reversible redox couple). The equilibrium values of the local surface concentrations are dictated by the potential distribution $V(Y)$ (eqs 11 and 12). When gradually increasing $\Delta\varphi_s$, one increases the local $V(Y)$, so the concentration differences, C_{Ox} and C_{R} , and the rates of the local mass transfer for Ox and R become larger in magnitude. Consequently, the surface concentration, $c_{\text{Ox}}(X=\pm 1, Y)$, progressively decreases (increases) for the left (right) part of the cell (Figure 3A–C). Changing the sign of $\Delta\varphi_s$ generates the expected permutation of the cathodic and anodic areas. The bulk concentration (at $X = 0$) drops due to depletion except for positions Y close to the injection point ($Y = 0$) where the bulk value is maintained. Steeper transversal depletion occurs when the lateral field is increased. As a result of the decrease of c_{Ox} at the surfaces with an increase of the potential $\Delta\varphi_s$ (Figure 5), the concentration gradients at the surfaces, and hence the local faradaic current densities $j(Y)$, increase in size. The overall current I_f , resulting from the spatial integration over the relevant surface areas of the current density $j(Y)$, follows the same trend. From a given value of $\Delta\varphi_s$, denoted as $\Delta\varphi_s^l$ (the superscript l pertains to the diffusion-limiting current condition), the faradaic processes at the extremities of the surfaces ($Y = 0$ and 1) are occurring at limiting rate. Ox species are reduced (and R oxidized) as fast as they can be brought to the electrode surfaces. Locally, the *diffusive limiting current* is reached, and the conductivity curve starts to develop a bend. Because the largest overpotentials ($V(Y) - V^*$) are located at $Y = 0$ and $Y = 1$, the current densities at these positions are the first to be affected by the limiting-

current condition (Figure 3D). For $\Delta\varphi_s \geq \Delta\varphi_s^l$, the limiting current is reached for larger fractions of the total cathodic and anodic areas (Figure 3D–I). In the extreme situation in which $\Delta\varphi_s \gg \Delta\varphi_s^l$, we have, for practically every Y , $j(Y) = j^l(Y)$. The concentration profile then presents a particular shape, as illustrated in Figure 3I. Applying the Leibnitz rule²³ to the second integral of eq 18, one can show that

$$\frac{dI_f}{d\Delta\varphi_s} = 2IL_0 \left\{ \int_{Y_0}^1 \frac{dj^l(Y)}{d\Delta\varphi_s} dY - j^l(Y=Y_0) \frac{dY_0}{d\Delta\varphi_s} \right\} \quad (21)$$

Because, under the limiting-current conditions, the applied pressure maintains $c_{\text{Ox}}(X=0, Y)$ at a constant value, $j^l(Y)$ remains independent of $V(Y)$ or, equivalently, $\Delta\varphi_s$. Using the definition adopted for Y_0 , one concludes that for $\Delta\varphi_s \gg \Delta\varphi_s^l$, I_f is approximately constant with respect to the applied $\Delta\varphi_s$ and equals I_f^l , as given by eq 18 after replacing $j(Y)$ and Y_0 by $j^l(Y)$ and Y_0^l , respectively. In the analysis, no other electron-transfer reactions than eq 2 are considered. However, in the limit of strong fields, reduction and oxidation of water also come into play,²² and this would obviously change the whole bipolar process. In the strong field limit ($\Delta\varphi_s \gg \Delta\varphi_s^l$), the potential distribution $V(Y)$ as formulated by eqs 14–17 asymptotically approaches linearity because $I_\Omega/I_f^l \gg 1$, I_Ω being the overall ohmic current. With this assumption, the limiting current density j^l is expected to depend on position according to the expression^{12,24}

$$j^l(Y) \propto Y^{-1/3} \tanh \left[\frac{nf}{2} \Delta\varphi_s (Y - Y_0^l) \right] \xrightarrow[\Delta\varphi_s \gg \Delta\varphi_s^l; Y < Y_0^l]{} -Y^{-1/3} \quad (22)$$

This is in very good agreement with the numerical results obtained, as illustrated in the inset of Figure 4A. A similar analysis cannot be straightforwardly performed for the positions $Y_0^l < Y \leq 1$ (anodic area) because there are no direct monopolar pendants for the corresponding concentration profiles (see below). Sections of various lateral positions Y of three-dimensional concentration profiles corresponding to $\Delta\varphi_s < \Delta$

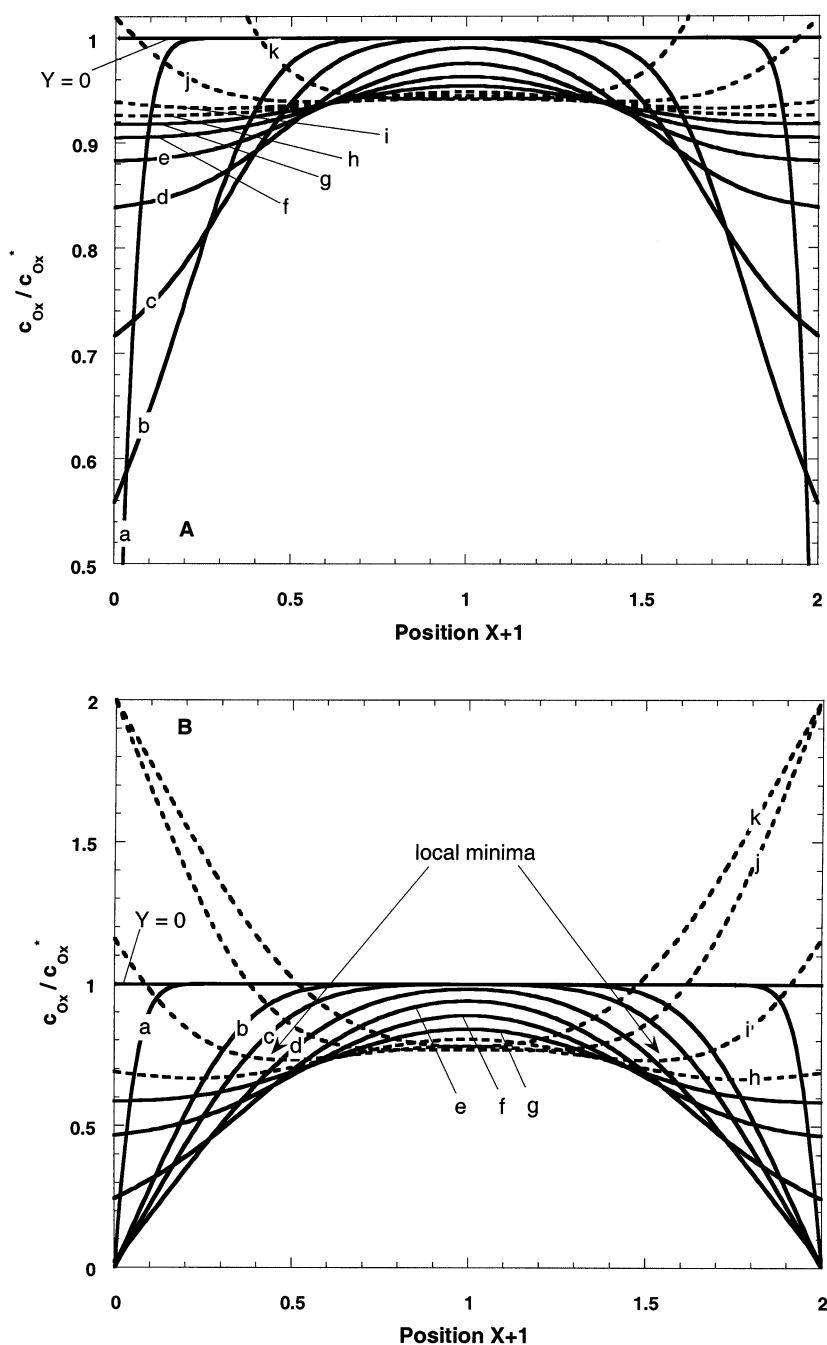


Figure 6. Cross sections at different positions Y of the concentration profiles c_{Ox}/c_{Ox}^* as pictured in (A) Figure 3C and (B) Figure 3G. Letters a–k refer to the positions $Y = 10^{-3}, 0.056, 0.111, 0.221, 0.331, 0.441, 0.551, 0.661, 0.771, 0.881$, and 0.991 . The dashed lines pertain to the positions Y where oxidation reaction takes place.

φ_s^l and $\Delta\varphi_s > \Delta\varphi_s^l$ are represented in panels A and B of Figure 6, respectively. Scanning the bipolar electrodes from their left sides to the position Y_0 (cathodic area), it is clear that the characteristic diffusion length δ increases to reach the value $a/2$ and that subsequently depletion of the oxidized species in the center of the cell occurs. Qualitatively, the observed dependence of δ on Y is in accordance with the trend predicted by Levich²⁴ in the Leveque approximation²⁵ for the simple case of a limiting diffusive flux in a laminar flow inside a monopolar circular tube. The dependence of δ on Y justifies that the limiting current density j^l , though independent of the potential distribution, remains a function of the lateral position Y (eq 22). The situation for $Y_0' \leq Y \leq 1$ is slightly more complicated. For sufficiently high $\Delta\varphi_s$, the current distribution in this Y -range

exhibits a peak with an amplitude that grows with the applied potential (Figure 4). The appearance of this peak is linked to the presence of a local minimum (the reasoning is made for $-1 \leq X \leq 0$) in the concentration profile of Ox (Figure 6), as resulting from the oxidation of R at the surfaces and the overshoot of R (as produced in the cathodic area and introduced by the flow for $Y > Y_0$) with respect to the position $X = 0$. The larger $\Delta\varphi_s$ is, the larger the overshoot in R and the Ox concentration at the surfaces becomes, and therefore the larger is the amplitude of the peak. Disappearance of the local minimum coincides with positions Y for which $j(Y)$ decreases. Upon increase of $\Delta\varphi_s$, the peaks are located at positions running from $Y = 1$ to Y_0' . This is in agreement with the direction according to which the spatial extension of the limiting-current

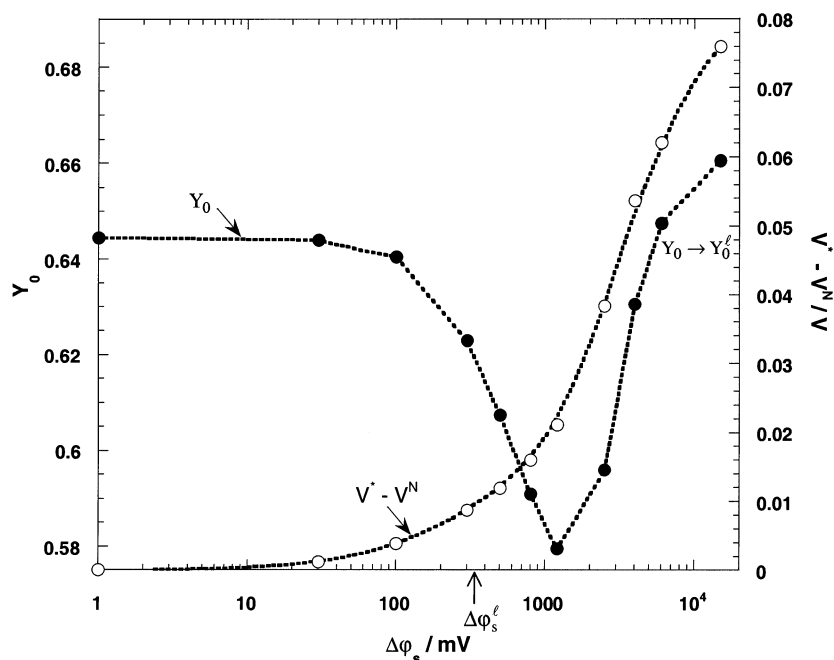


Figure 7. Asymmetry of the bipolar process as induced by the applied field $\Delta\varphi_s$ at constant pressure ($\Delta P = 0.5$ kPa). Model parameters are as follows: $a = 0.2$ mm; $L_0 = 7.6$ cm; $l = 2.6$ cm; $D = 10^{-9}$ m² s⁻¹; $V^0 = -233$ mV; $K^L = 1$ Ω⁻¹ m⁻¹; $c_{\text{Ox}}^* = c_{\text{R}}^* = 0.1$ mM.

condition takes place in the cathodic and anodic areas with increasing $\Delta\varphi_s$.

For the particular pressure considered, the current and potential distributions present a certain asymmetry with respect to the position halfway the electrode ($Y = 0.5$). This is directly related to the asymmetrical spatial distribution of the diffusion layer thickness, $\delta(Y)$, which, in turn, gives rise to huge variations of Y_0 with changing ΔP (see next section). The amplitude of these variations depends to a minor extent on the electric field (Figure 7). To ensure the balance between the total anodic and cathodic currents, upon increase of $\Delta\varphi_s$, the position Y_0 moves first slightly to lower values and then to higher ones to tend to Y_0' . The initial decrease corresponds to the potential regime in which the growth of the local cathodic currents with the applied field is stronger than that for the local anodic currents. The increase appears at $\Delta\varphi_s$ values for which the cathodic process is critically limited by diffusion in the sense that Y_0 shifts to the anodic area to counterbalance the ongoing increase of the overall oxidation current, predominantly due to the increasing overshoot of R (current peak). The values of the potential V^* corresponding to the different positions Y_0 are also indicated. Contrary to the bipolar processes analyzed in ref 14, V^* is not simply given by the Nernst potential (eq 20) of the original solution with the concentrations c_{Ox}^* and c_{R}^* but by an increasing function of the electric potential in solution which, as we shall see in the next paragraph, also depends on the mass-transfer conditions.

2.4.2. Analysis at Given Lateral Field $\Delta\varphi_s$ and Various Pressures ΔP (Inset Figure 2). Let us analyze more specifically the influence of the applied pressure on the bipolar process. For this purpose, snapshots of the concentration profile for the Ox species are given for different ΔP and constant $\Delta\varphi_s$ (Figure 8). The spatial distributions of the local faradaic current and the potential, as well as the characteristic values of Y_0 and V^* , are shown in Figure 9. For every X , the velocity at which the electroactive species are transported along the surface is scaled with ΔP (eqs 6–7). For very low ΔP , the lateral convection is so weak that the bulk concentration c_{Ox}^* is only maintained close to the injection point ($Y = 0$) and within a certain range

of X , which also depends on the applied potential (see Figure 5). The cathodic process is confined to the extreme left side of the electrodes ($Y_0 \approx 0$ and $V^* \approx \Delta\varphi_s + V^N$), so oxidation reaction takes place over practically the whole range of Y values ($V(Y) < V^*$) with a gradual change of c_{Ox} (Figure 8A). The local currents and the corresponding overall bipolar current are so low that the potential distribution is practically linear ($I_f \ll I_\Omega$). With increasing ΔP , the magnitude of the cathodic area increases ($dY_0/d\Delta P > 0$), and the fraction of the total applied potential span along the anodic side of the electrode decreases ($dV^*/d\Delta P < 0$). This corresponds to a translation of the spatial distribution of $(V(Y) - V^*)$ toward more positive values, which is combined with a deformation of the profile with respect to linearity (see Figure 9C). Indeed, at both extremities of the cell, the electric-field strength increases (eq 17), as can be inferred from the corresponding slopes $dV(Y)/dY$. This is due to the increase of the current $j(Y)$ for $Y = 0$ and $Y = 1$, as resulting from the decreasing δ (Figure 8B–F) with ΔP . In the previous section, the conductivity curve could be interpreted by considering, for a fixed position Y along the electrode and a given ΔP , the change of $j(Y)$ upon the effect of $V(Y)$ as induced by variation of $\Delta\varphi_s$. In the current analysis, $j(Y)$ is affected not only by the pressure but also by the corresponding significant local variations of the potential $V(Y)$, resulting from the enhanced spatial asymmetry of the bipolar process. Upon increase of ΔP , the thickness of the diffusion layer δ for every Y decreases. This means that for any Y , the window of X values where lateral convection prevails becomes wider, with the concentration approaching the value c_{Ox}^* (Figure 10A). The effect of the pressure on $\delta(Y)$ enlarges the concentration gradient at the surface, and hence, the current density $j(Y)$ at the positions where the electric field strength E is the largest, that is, at the left and right sides of the cell. It results in a steep increase of the bipolar current (eq 19), as illustrated in the inset of Figure 2. One can verify that, for the (very low) ΔP and $\Delta\varphi_s$ ranges corresponding to potential distributions that do not significantly deviate from linearity, I_f varies according to the power law $\Delta P^{1/3}$, as found in ref 12. As a result of the concomitant shift of $(V(Y) - V^*)$

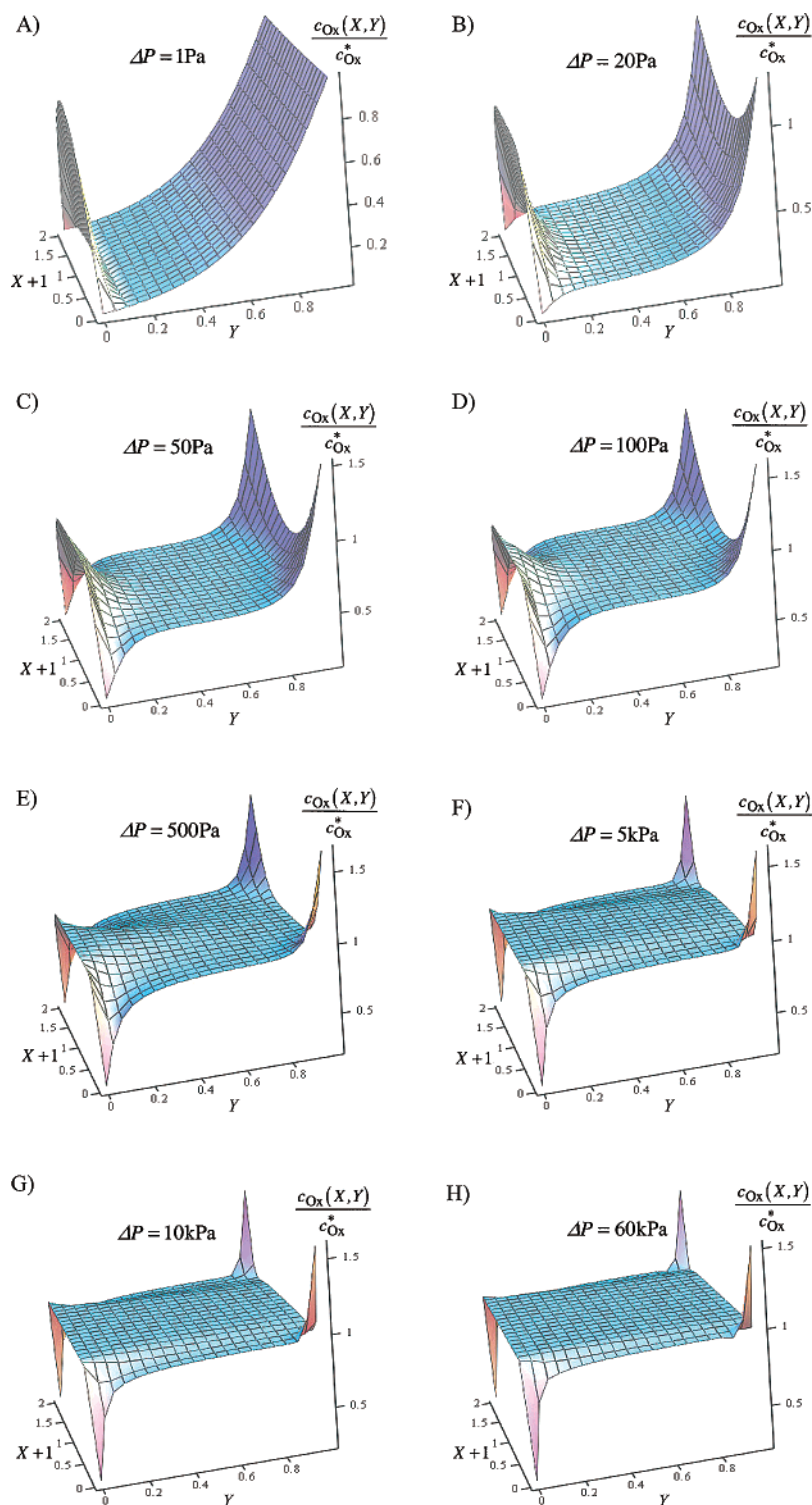


Figure 8. Concentration profiles of the oxidized form of the redox couple at varied applied pressures ΔP (indicated) and constant applied field $\Delta\varphi_s = 100$ mV (section 2.4.2). Model parameters are as follows: $a = 0.2$ mm; $L_0 = 7.6$ cm; $l = 2.6$ cm; $D = 10^{-9}$ m² s⁻¹; $V^0 = -233$ mV; $K^L = 1$ Ω⁻¹ m⁻¹; $c_{Ox}^* = c_R^* = 0.1$ mM. The profiles at the injection position $Y = 0$ (left extremity of the cell) are not drawn ($c_{Ox} = c_{Ox}^*$).

and the increase of E at the extremities of the surfaces, the potential gradient flattens in the midrange of Y . The corresponding local E and the current density $j(Y)$ are lowered. The spatial range involved with the suppression of the field increases with the pressure. Quantitatively, the increase of E at the extremities is large enough to compensate for the decreasing $j(Y)$ in the midrange, so the overall bipolar current I_f keeps on growing but to a lesser extent than that for low ΔP . I_f then varies according to the power law $\Delta P^{1/\beta}$ with $\beta \approx 5$ (see fits in

the insert Figure 2), which is in agreement with the deviation expected on the basis of the assumption of a linear potential distribution (for which $\beta = 3$). The simultaneous dependencies of $j(Y)$ on the hydrodynamic and electric parameters explain the existence of extrema reached by j and by the local E for certain positions Y along the electrode, as shown in Figure 10B. Referring to this figure, in the ΔP -region (I), $j(Y)$ increases even though the driving field decreases (in absolute value): this is mainly attributed to the decrease of $\delta(Y)$; in region II, the

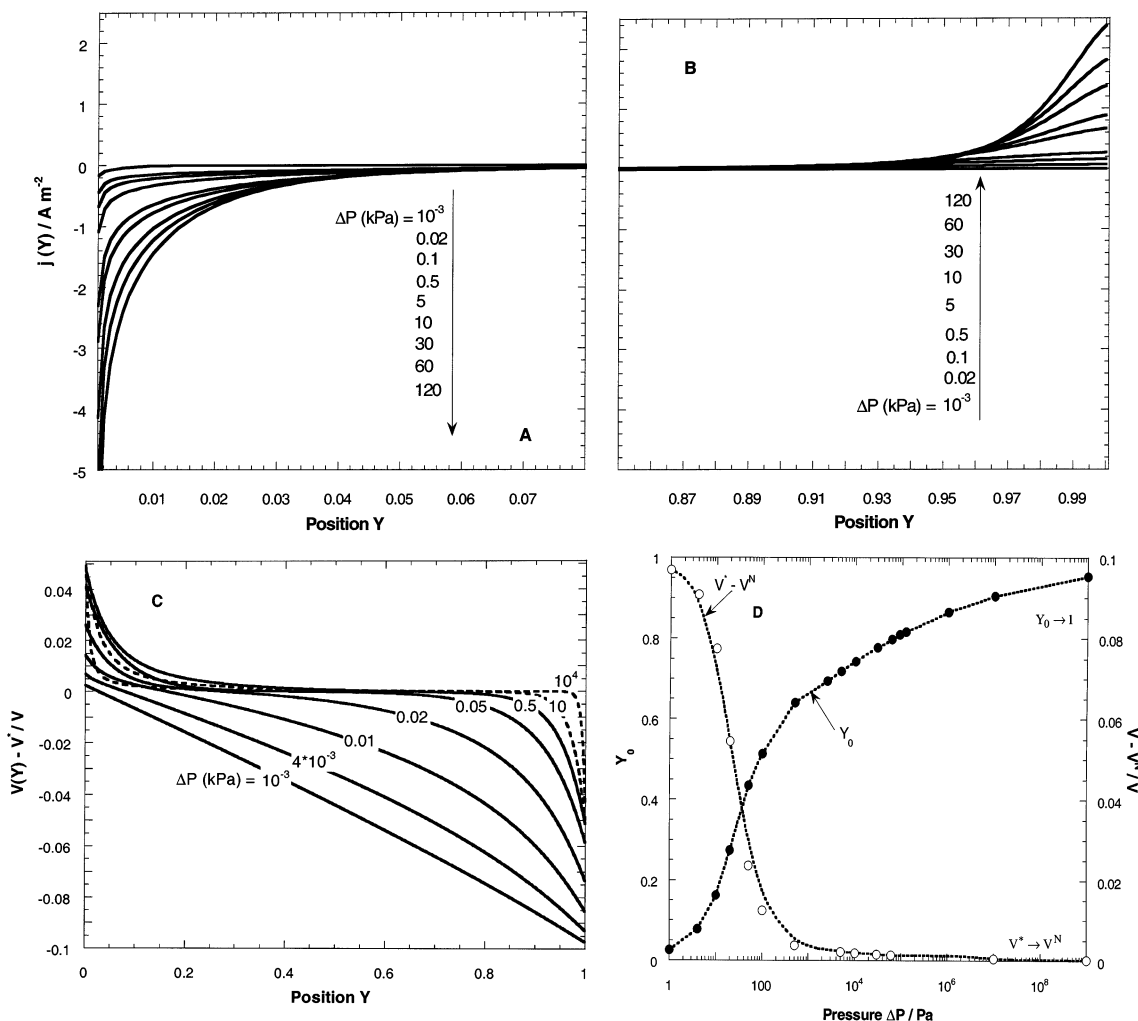


Figure 9. Spatial distributions of the local faradaic current density $j(Y)$ (panel A, reduction current; panel B, oxidation current) and the local potential $V(Y)$ (panel C) along the conducting surface at varied ΔP (indicated) and constant $\Delta\varphi_s = 100$ mV. In panel D, the corresponding parameters Y_0 and V^* are given. Model parameters are as follows: $a = 0.2$ mm; $L_0 = 7.6$ cm; $l = 2.6$ cm; $D = 10^{-9}$ m² s⁻¹; $V^0 = -233$ mV; $K^L = 1$ Ω^{-1} m⁻¹; $c_{Ox}^* = c_R^* = 0.1$ mM.

pressure is such that cathodic reaction now takes place ($Y < Y_0$); the increasing field and decreasing $\delta(Y)$ are both responsible for the increase of the current (in absolute value); in region III, the decrease of $V - V^*$ results in the decrease of $j(Y)$. In the limit of very high pressure, the anodic reaction is in turn spatially confined at the extreme right side of the electrode ($Y_0 \rightarrow 1$ and $V^* \rightarrow V^N$), and the cathodic reaction spans over the entire Y -range. The effective overpotential ($V(Y) - V^*$) and the current $j(Y)$ tend to small values over the whole Y -range except at the very edges, where there is a drastic increase of E and j . The concentration profiles present sharp peaks at the position $Y = 0, 1$ and $X = -1, 1$ (Figure 8G,H).

2.4.3. Dependence of the Bipolar Current I_f on c_{Ox}^*/c_R^* , K^L , and a . Figure 11A illustrates the effect of the bulk redox concentrations on the conductivity curves. As expected, I_f increases with increasing c_{Ox}^* or c_R^* or both and is limited by the lower of the two concentrations. Because of the nonlinear coupling between local current and potential, I_f does not depend linearly on the bulk concentrations.¹⁴ A ratio $c_{Ox}^*/c_R^* \neq 1$ induces a spatial asymmetry for the bipolar process and hence a shift of the position Y_0 . The potential distribution tends to linearity for low c_{Ox}^* or c_R^* or both, corresponding to low I_f with respect to the ohmic current I_Ω (Figure 11B). A comparable picture can be given when varying the bulk conductivity of the solution K^L or the cell dimension a (Figures 12 and 13). With

increasing K^L or a , the local potential $|V(Y)|$ and hence the overall current I_f increase. In the meantime, the ratio I_Ω/I_f grows and the potential distribution approaches linearity.

2.4.4. Application to the Electrokinetics of the Metal/(Electroactive) Solution Interface. In the frame of streaming potential experiments, a potential difference is built up across the cell upon application of a pressure drop ΔP along the surface. This results from the lateral displacement of the mobile part of the counter charge at the interface substrate/solution. When the solution contains electroactive species and the surfaces are conducting, this potential, called the streaming potential $\Delta\varphi_{str}$, induces a bipolar electrodynamic behavior of the surfaces in the same way as described in section 2.1. In steady-state, the net-current flow in the channel is zero; the streaming current I_{str} caused by the forced convection of solution stripping charge along the double layer is then counterbalanced by the total current I flowing in the cell ($I_{str} + I = 0$ with I_{str} and I algebraic currents). I contains a surface conduction contribution and a bulk contribution depending on the electric field as determined by the coupling between conduction and faradaic currents (see eq 14). For the geometry considered in this paper, I is written

$$I = (aK^L + 2K^\sigma)l \left. \frac{\partial V}{\partial y} \right|_{y=L_0/2} \quad (23)$$

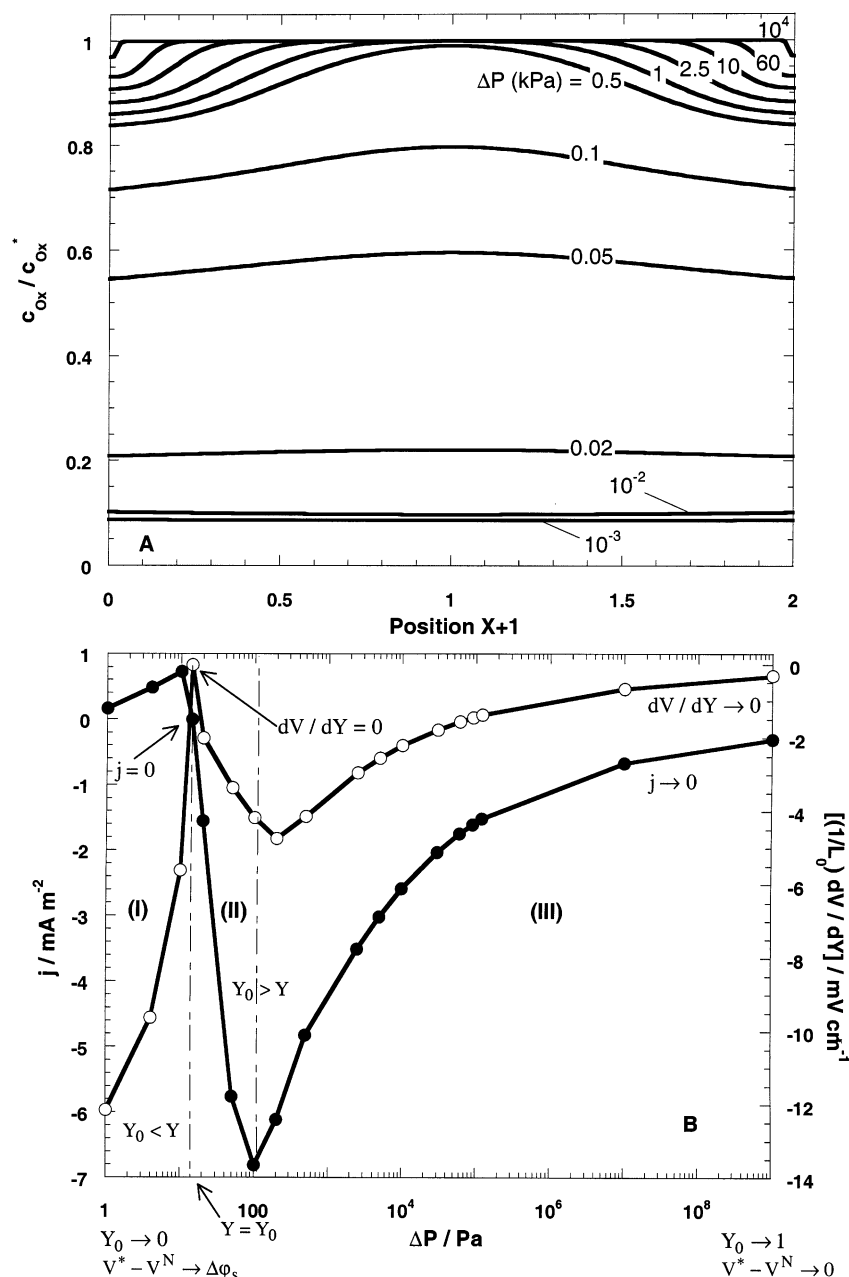


Figure 10. Cross sections (A) of the concentration profiles c_{Ox}/c_{Ox}^* represented in Figure 8 at the position $Y = 0.221$ providing an illustration of the decrease of the diffusion length δ and of the increase of the concentration $c_{Ox}(X=0, Y)$ with increasing ΔP (indicated in kPa). Panel B shows the Faradaic current density $j(Y=0.221)$ and local electric field strength $E(Y=0.221)$ as a function of the pressure (see text). Panel B uses the same parameters as panel A.

K^σ being the surface conductivity. Using eq 19, we can rearrange eq 23 as follows:

$$I = -I_f(\Delta\varphi_{str}, \Delta P) + alK^L \left. \frac{\partial V}{\partial y} \right|_{y=y_0} + K^\sigma \left(-\frac{2I_f(\Delta\varphi_{str}, \Delta P)}{aK^L} + 2l \left. \frac{\partial V}{\partial y} \right|_{y=y_0} \right) \quad (24)$$

I_f is the bipolar current depending on the electric and hydrodynamic variables, $\Delta\varphi_{str}$ and ΔP . The streaming current is yielded by²⁶

$$I_{str} = 2l \int_{a/2}^a \rho(x) v(x) dx = \frac{al\epsilon_0\epsilon_r \zeta \Delta P}{\eta L_0} \quad (25)$$

ζ being the electrokinetic potential (ζ -potential), ϵ_0 the dielectric permittivity of vacuum, and $\rho(x)$ the local ionic charge density coupled to the potential distribution at the interface, as expressed by the Poisson–Boltzmann equation. Within the framework of the current study, it is assumed that the surface conduction contribution is either absent or negligible with respect to the other conduction terms so that the condition $I_{str} + I = 0$ becomes

$$\frac{\epsilon_0\epsilon_r \zeta \Delta P}{\eta} = -L_0 K^L \left. \frac{\partial V}{\partial y} \right|_{y=y_0} + \frac{L_0}{al} I_f(\Delta\varphi_{str}, \Delta P) \quad (26)$$

One verifies that in the absence of faradaic depolarization (i.e., $I_f = 0$ and $\partial V/\partial y|_{y=y_0} = -\Delta\varphi_{str}/L_0$), eq 26 reduces to the classical Helmholtz–Smoluchowski equation. The potential $\Delta\varphi_s$ span along the surfaces is now the potential, as generated by the flow,

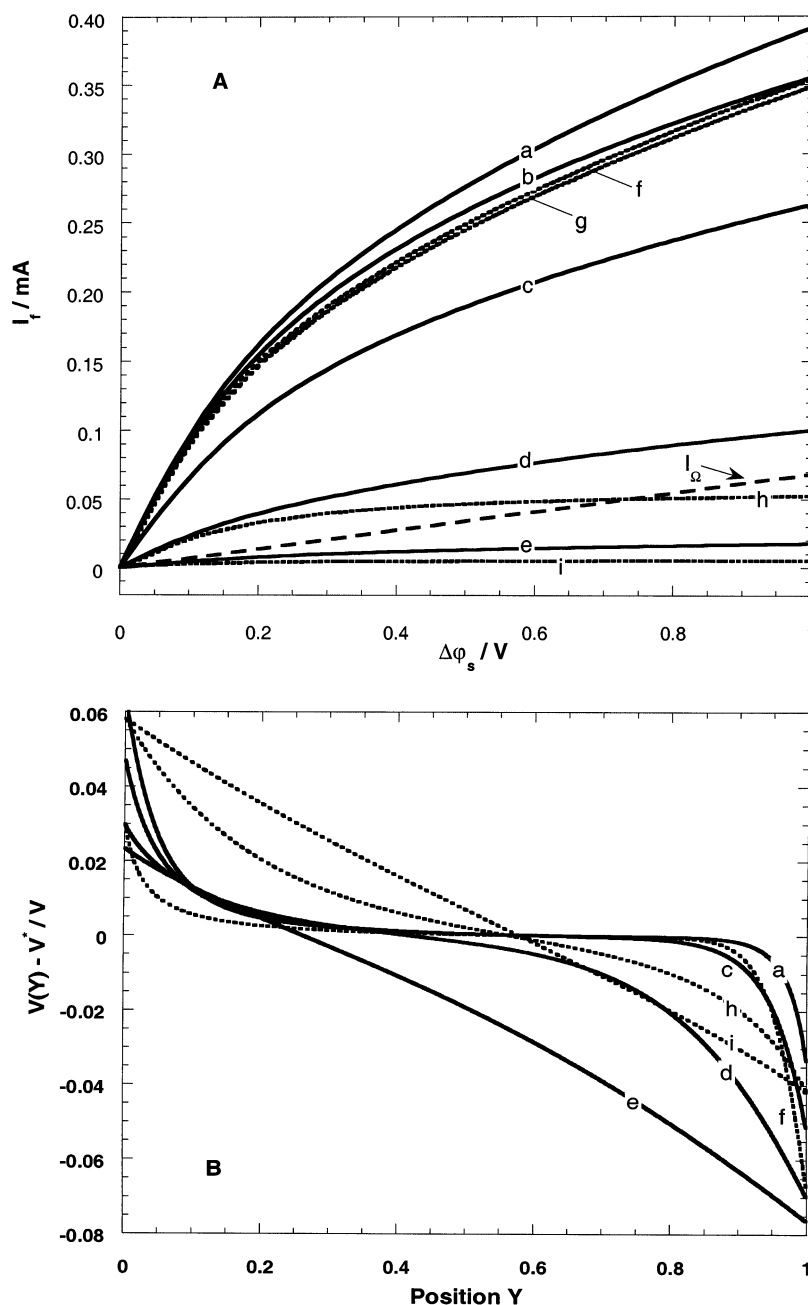


Figure 11. Bipolar current (A) as a function of the applied field for different sets of redox concentrations at constant pressure $\Delta P = 0.5$ kPa. The ohmic current I_Ω is indicated for comparison purposes. Panel B shows the corresponding spatial distributions of the potential at $\Delta\phi_s = 100$ mV. Plain lines present $c_{\text{Ox}}^* = 10^{-4}$ M and $c_{\text{R}}^* =$ (a) 10^{-2} M, (b) 10^{-3} M, (c) 10^{-4} M, (d) 10^{-5} M, and (e) 10^{-6} M. Dashed lines present $c_{\text{R}}^* = 10^{-4}$ M and $c_{\text{Ox}}^* =$ (f) 10^{-2} M, (g) 10^{-3} M, (h) 10^{-5} M, and (i) 10^{-6} M. Model parameters are as follows: $a = 0.2$ mm; $L_0 = 7.6$ cm; $l = 2.6$ cm; $D = 10^{-9}$ m² s⁻¹; $V^0 = -233$ mV; $K^L = 1$ Ω^{-1} m⁻¹.

and related to the double-layer properties of the interfaces. For given concentrations of the electroactive species, once steady state is reached, we have

$$I_f(\Delta\phi_{\text{str}}, \Delta P) \equiv I_f(\Delta\phi_s = \Delta\phi_{\text{str}}, \Delta P) \quad (27)$$

meaning that, basically, the bipolar current generated by the streaming potential $\Delta\phi_{\text{str}}$ resulting from the pressure ΔP is the same as the one that would be obtained by externally applying the same pressure and a potential difference $\Delta\phi_s = \Delta\phi_{\text{str}}$.

Given some characteristics of the electrolyte solution (K^L , c_{Ox}^* , c_{R}^*), the bipolar current I_f was first computed for a given ΔP in a potential range $\Delta\phi_s$ compatible with electrokinetic experiments (0–70 mV). The resulting conductivity curve I_f

($\Delta\phi_s, \Delta P$) was fitted by polynomial regression and use of the least-squares method. Assuming a given ζ -potential, the streaming potential $\Delta\phi_{\text{str}}$ corresponding to the pressure ΔP considered was calculated by solving eqs 26 and 27 assuming a priori that $\partial V / \partial y|_{y=y_0} = 0$. It was a posteriori verified that taking into account the first term in the rhs of eq 26 does not change the solution obtained. To reconstruct the $\Delta\phi_{\text{str}} - \Delta P$ plot, this procedure was repeated for various pressures ΔP . A graphical illustration is given in Figure 14 (panel B), which also shows typical $\Delta\phi_{\text{str}} - \Delta P$ plots obtained (panel A). The bipolar faradaic current strongly curbs the generation of the streaming potential, and this is reflected by considerable deviations (also for low pressures) from the results expected on the basis of the linear H–S equation. As a result of the nonlinear pressure dependence

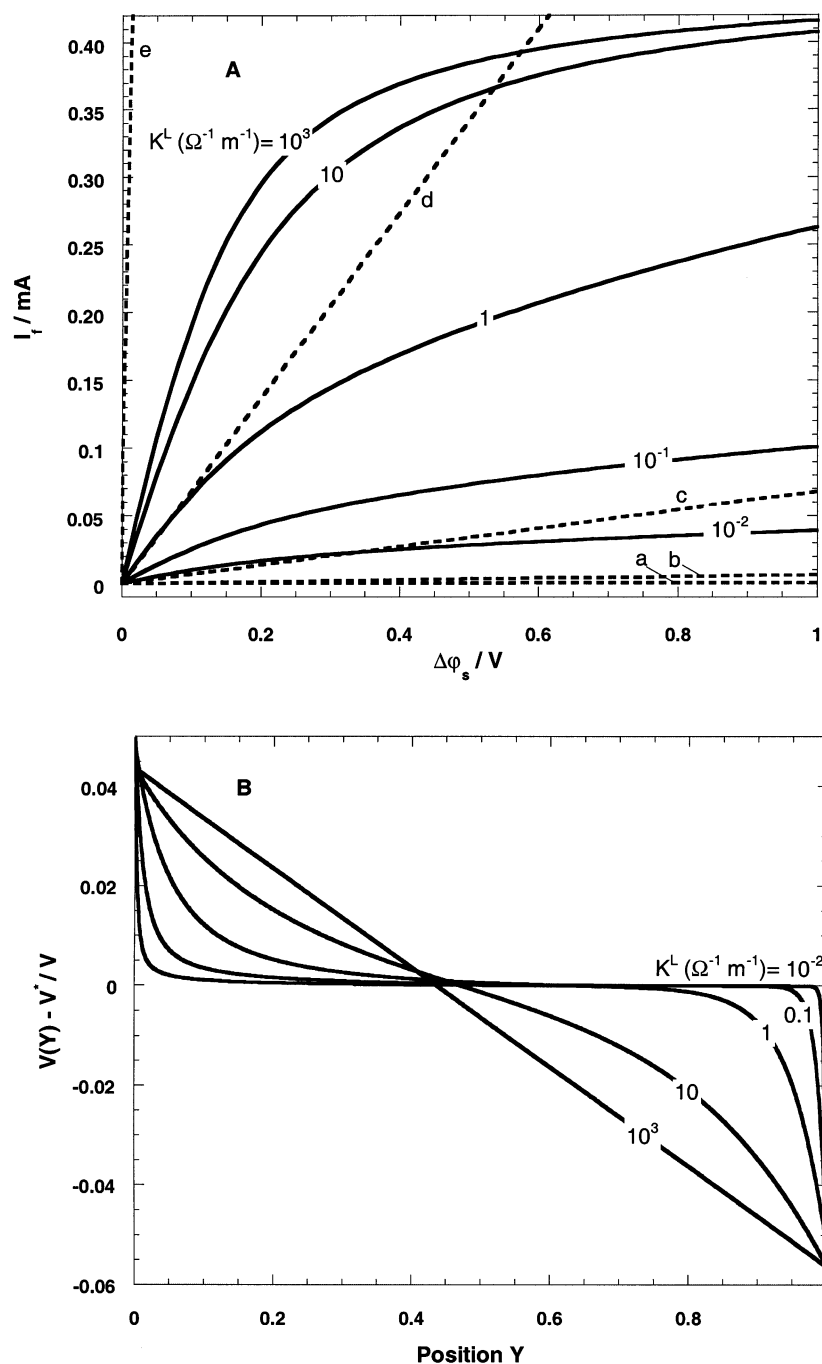


Figure 12. Bipolar current (A) as a function of the applied field for different K^L (indicated) at constant pressure $\Delta P = 0.5$ kPa. The corresponding ohmic currents I_Ω (dashed curves a–e for low to high K^L) are given. Panel B presents the corresponding spatial distributions of the potential at $\Delta\phi_s = 100$ mV. Model parameters are as follows: $a = 0.2$ mm; $L_0 = 7.6$ cm; $l = 2.6$ cm; $D = 10^{-9} \text{ m}^2 \text{ s}^{-1}$; $V^0 = -233$ mV; $c_{\text{Ox}}^* = c_{\text{R}}^* = 0.1$ mM.

of I_f on ΔP for the entire pressure range examined, the $\Delta\phi_{\text{str}} - (\Delta P)$ curves develop a bend (in the example given, at $\Delta P \approx 40$ kPa). For higher ΔP (> 40 kPa), the $\Delta\phi_{\text{str}} - \Delta P$ plots progressively reach a linear regime. Indeed, for given (K^L , c_{Ox}^* , c_{R}^*), the magnitude of the lateral field met in electrokinetic experiments is so low that I_f depends linearly on $\Delta\phi_s \equiv \Delta\phi_{\text{str}}$ (see Figure 2). Besides, in the high-pressure range, the bipolar current weakly increases when increasing ΔP , and the corresponding dependence $I_f \propto (\Delta P)^{1/\beta}$ can be legitimately approximated to a straight line (see inset Figure 2). As a result, the bipolar conductivity remains practically constant in the high-pressure and low-potential ranges. This feature may be particularly useful for the treatment of experimental data.¹⁹ To illustrate the necessity of considering a nonlinear spatial distribution for the

potential in the determination of I_f , $\Delta\phi_{\text{str}} - \Delta P$ plots were calculated in the condition of Figure 14A with the expression for I_f based on the assumption of constant field along the surfaces.¹² As expected, this assumption leads to overestimation of I_f and underestimated values for $\Delta\phi_{\text{str}}$ as compared with those obtained from the rigorous numerical analysis.

A detailed analysis of experimental data for the gold/(Fe(CN)₆³⁻/Fe(CN)₆⁴⁻, KNO₃) interface, in conjunction with an outline of the nature of the ζ -potential in the presence of a redox couple, is given elsewhere.¹⁹

3. Conclusions

The bipolar behavior of metallic surfaces in a thin-layer cell of the type used for electrokinetic experiments is described in

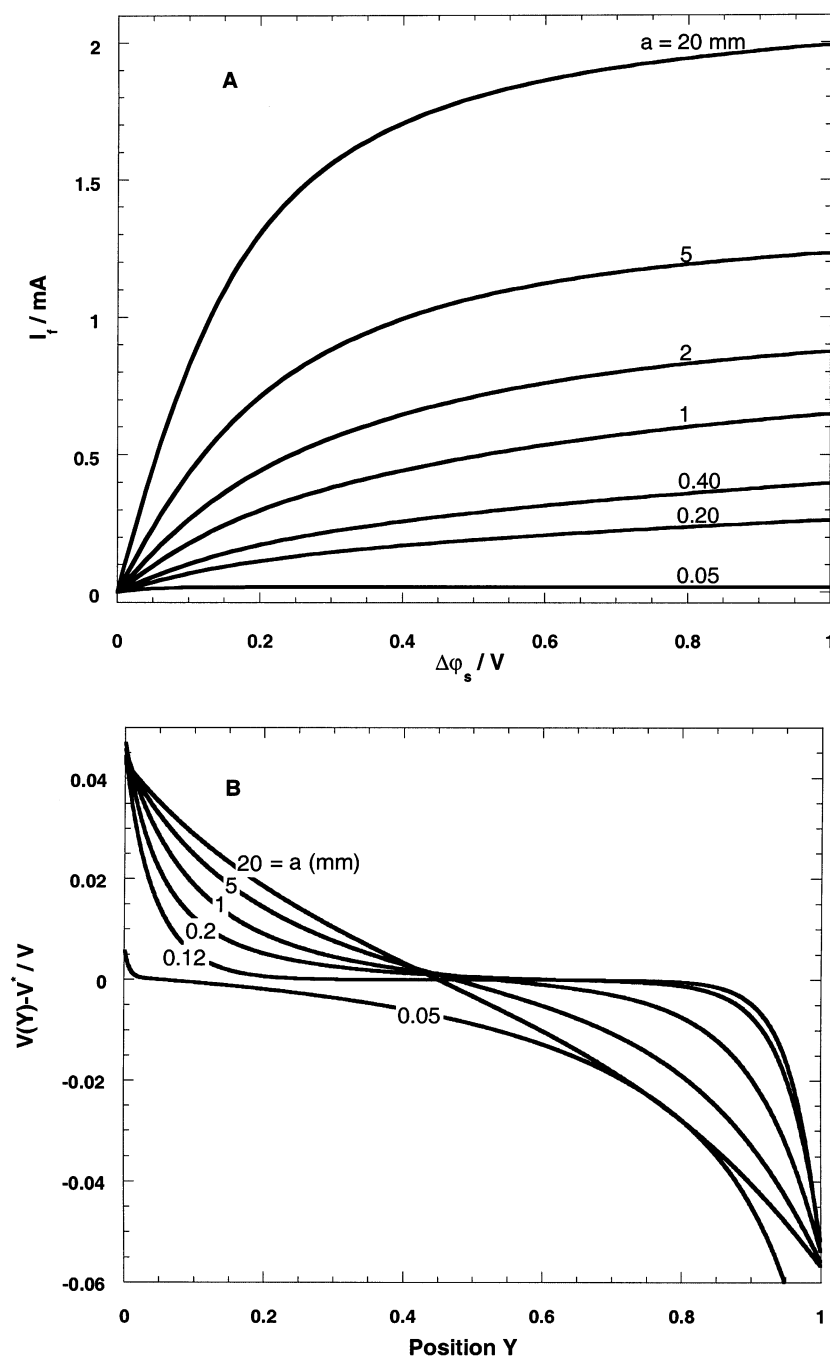


Figure 13. Bipolar current (A) as a function of the applied field for different a (indicated) at constant pressure $\Delta P = 0.5$ kPa and (B) Corresponding spatial distributions of the potential at $\Delta\phi_s = 100$ mV. Model parameters are as follows: $L_0 = 7.6$ cm; $l = 2.6$ cm; $D = 10^{-9}$ m² s⁻¹; $V^0 = -233$ mV; $K^L = 1$ Ω^{-1} m⁻¹; $c_{\text{Ox}}^* = c_{\text{R}}^* = 0.1$ mM.

the situation in which the faradaic depolarization of the interface is induced by convective diffusion-controlled electron-transfer reactions. The typical pattern of the conductivity curves is interpreted in terms of the corresponding spatial distribution of the concentration polarization of the electroactive species along the conducting surface, the local faradaic current density, and the electric field. These were calculated by numerical analysis of the intrinsically coupled Nernst–Planck equation and Poisson equation for finite currents. The bipolar current I_f levels off and asymptotically reaches a constant value at strong lateral fields, resulting from diffusion limitation of the local electron transfer. I_f weakly increases at high applied pressure gradients because of the enhanced spatial asymmetry of the bipolar process. The bulk substrate faradaic conduction is more significant with

respect to the bulk solution conduction at low applied potential differences and low applied pressure gradients across the cell because these correspond to the steepest variations in I_f . The subtle combination between electric and hydrodynamic variables in the determination of the overall bipolar current yields characteristic nonlinear distribution for the local potential along the surface (even at low applied fields). In view of the complexity of the problem, full description of the phenomenon cannot be reduced to a simple analysis based on the assumption of a linear field, which at most provides only a rough estimate of the bipolar current. The steady-state theory developed for the computation of the bipolar faradaic conductivity under given applied field and pressure may be used in the quantitative interpretation of electrokinetic measurements performed on

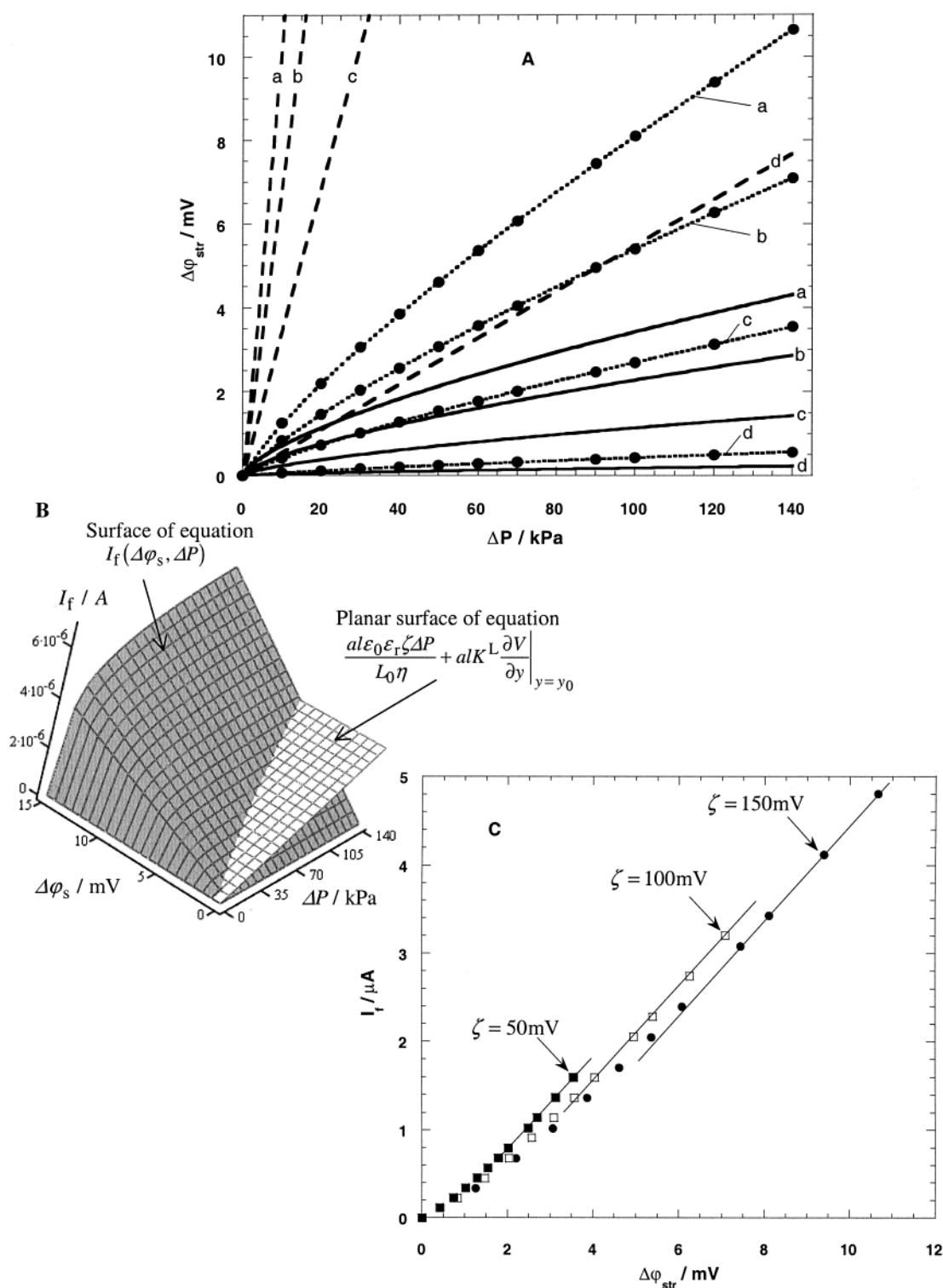


Figure 14. Reconstruction (A) of the $\Delta\phi_{\text{str}}-\Delta P$ plots (points) for $\zeta =$ (a) 150 mV, (b) 100 mV, (c) 50 mV, and (d) 8 mV. The corresponding curves calculated on the basis of the linear H-S equation (no Faradaic depolarization taken into account) and of the assumption of a uniform field¹² are indicated in dashed and plain lines, respectively. Panel B presents a graphical interpretation of the computational procedure followed for the determination of the $\Delta\phi_{\text{str}}-\Delta P$ plots (the example is given for $\zeta = 100 \text{ mV}$). In panel C, the points refer to the $(I_f, \Delta\phi_{\text{str}})$ of curves a, b, and c of panel A and computed with the nonuniform field theory. The lines are linear fits in the high-pressure regime (see text). Parameters (common to panels A, B, and C) are as follows: $a = 1 \text{ mm}$; $L_0 = 7.6 \text{ cm}$; $l = 2.6 \text{ cm}$; $D = 5 \times 10^{-10} \text{ m}^2 \text{ s}^{-1}$; $V^0 = -233 \text{ mV}$; $K^L = 0.1 \Omega^{-1} \text{ m}^{-1}$; $c_{\text{Ox}}^* = c_{\text{R}}^* = 10^{-5} \text{ M}$.

metals in electroactive solution. In such measurements, the electric driving field for faradaic depolarization of the interface is coupled to the pressure, as imposed by the nonlinear Helmholtz-Smoluchowski equation. Assuming a given ζ -potential, a computational procedure is proposed to reconstruct the nonlinear streaming potential/pressure plots.

This paper shows that it is possible to electrokinetically probe double-layer properties of metals in the presence of a reversible redox couple, provided any accompanying bipolar depolarization is well understood and taken into proper account. More specifically, it is shown that electrokinetic experiments may allow assessment of the dependence of the ζ -potential on the

total potential drop across the metal/solution interface, which can be electrochemically manipulated via the concentrations of the redox species in the solution. Such type of investigation has not yet been envisaged in the field of electrokinetics, neither experimentally nor theoretically.

Examination of bipolar faradaic depolarization inherent to the electrokinetics of spherical metallic particles submitted to high electric fields will be reported later. It will be shown that a judicious choice of the electrolyte may allow occurrence of superfast electrophoresis at fields commonly applied in standard electrophoresis experiments.

Acknowledgment. This work was carried out within the frame of the project Electrophoretic Particle Deposition with financial support from SENTER (Dutch ministry of Economic Affairs).

Appendix

Computation of the Concentration Profiles $c_{\text{ox}}(X,Y)$, the Spatial Distributions of the Potential $V(Y)$, and the Local Faradaic Current Density $j(Y)$. Contrary to the study made of the transient characteristics for diffusion-limited bipolar processes,¹⁴ decoupling of the transport eq 9 and the Poisson eq 14 in the current problem cannot be simply performed by analytical means. Therefore, a consistent numerical solution of the complete set of eqs 9–12 and 14–17 must be found.

Discretization of the Convective Diffusion Equation. The problem is symmetrical with respect to $X = 0$, so in the following, the analysis will be restricted to the interval $0 \leq X \leq 1$. The corresponding boundary conditions, as associated to eq 9 in the text, are

$$C_{\text{ox}}(X=+1,Y) = Q(Y) \quad (\text{A1})$$

$Q(Y)$ being given by eq 11, and

$$\left. \frac{\partial C_{\text{ox}}(X,Y)}{\partial X} \right|_{X=0} = 0 \quad (\text{A2})$$

The spatial variables X and Y are written

$$i \in [1,M] \quad X_i = (i-1)\Delta X \quad (\text{A3})$$

$$k \in [1,N] \quad Y_k = (k-1)\Delta Y \quad (\text{A4})$$

where M and N are integers and ΔX and ΔY are the spatial steps for the X and Y directions, respectively. For the sake of simplicity, we write $C_{\text{ox}}(X_i,Y_k) = C_{i,k}$ and $Q(Y_k) = Q_k$. To optimize the convergence of the solution and reduce the computation time, the inverse-Euler method²⁷ was chosen for discretizing eqs 9, A1, and A2. For a given position Y_k , this comes to

$$i \in [2,M-1]$$

$$-r_i C_{i-1,k-1} + (1+2r_i)C_{i,k+1} - r_i C_{i-1,k+1} = C_{i,k} \quad (\text{A5})$$

$$C_{1,k+1} - C_{2,k+1} = 0 \quad (\text{A6})$$

$$C_{M,k+1} - Q_{k+1} = 0 \quad (\text{A7})$$

r_i being the quantity defined by

$$i \in [2,M-1] \quad r_i = \frac{4DL_0}{v^0 a^2} \frac{\Delta Y}{[1 - (i-1)^2 \Delta X^2] \Delta X^2} \quad (\text{A8})$$

Equations A5–A8 can be written for every k in the matricial form

$$k \in [1,N] \quad T \cdot \vec{C}_{k+1} = \vec{C}_k \quad (\text{A9})$$

\vec{C}_{k+1} and \vec{C}_k being the column vectors

$$\vec{C}_{k+1} = \begin{pmatrix} C_{1,k+1} \\ C_{2,k+1} \\ C_{3,k+1} \\ \vdots \\ C_{M,k+1} \end{pmatrix} \quad \vec{C}_k = \begin{pmatrix} 0 \\ C_{2,k} \\ C_{3,k} \\ \vdots \\ C_{M-1,k} \\ Q_{k+1} \end{pmatrix} \quad (\text{A10})$$

and T being the trigonal matrix of dimension $M \times M$

$$T = \begin{pmatrix} 1 & -1 & 0 & & 0 \\ -r_2 & 1+2r_2 & -r_2 & & \\ 0 & -r_3 & 1+2r_3 & -r_3 & 0 \\ & & & & 0 \\ & & & -r_{M-1} & 1+2r_{M-1} & -r_{M-1} \\ 0 & & & 0 & 0 & 1 \end{pmatrix} \quad (\text{A11})$$

To solve eq A9 for every k , values of the components $(Q_k)_{k \in [1,N]}$ of the column vector \vec{Q} are required. \vec{Q} depends on the potential distribution $(V(Y_k))_{k \in [1,N]} = (V_k)_{k \in [1,N]}$ as formulated by eqs 14–17. The potentials $(V_k)_{k \in [1,N]}$ are coupled to the local concentration profiles via the local faradaic current density $(j(Y_k))_{k \in [1,N]} = (j_k)_{k \in [1,N]}$ defined by

$$k \in [1,N] \quad j_k = \frac{2nFDc_{\text{ox}}^*}{a\Delta X} (C_{M,k} - C_{M-1,k}) \quad (\text{A12})$$

For every k , the $C_{i,k}$ are linear with respect to the Q_k . Physically, this means that the concentration profile scales with the surface concentration for every position along the surface (i.e., the shape of the profile does not depend on the actual values of c_{ox}^* and c_{r}^*). Because the local current density is linearly related to the gradient of the concentration at the surface (eq A12), one infers the existence of a linear relationship between the j_k and the Q_k . Denoting \vec{j} the column vector of components $(j_k)_{k \in [1,N]}$, we conclude that there is a matrix A of dimension $N \times N$ such that

$$\vec{j} = A \cdot \vec{Q} \quad (\text{A13})$$

Because the components of the matrix T only depend on the index i , the constitutive elements of A are independent of k . Because of this property, relation A13 allows decoupling of eqs 9–12 (A9) and eqs 14–17, as we shall demonstrate in the following.

Calculation of the Matrix A . Let \mathcal{F} be a numerical solver that enables the calculation of the searched \vec{C}_k from a known solution \vec{C}_{k-1} and a given vector \vec{Q}

$$k \in [1,N] \quad \vec{C}_k = \mathcal{F}(\vec{C}_{k-1}, \vec{Q}) \quad (\text{A14})$$

Iterating k from 1 to N with $\vec{C}_0 = \vec{0}$ as starting solution, we can obtain the $(C_{i,k})_{i \in [1,M], k \in [1,N]}$ and hence the $(j_k)_{k \in [1,N]}$. The numerical method as subsumed in \mathcal{F} for solving the linear algebraic trigonal system (eq A9) is based on a simple form taken by the classical Gaussian elimination technique with partial pivoting.²⁸

Let us consider N sets of solutions $(\vec{C}_k^{*(n)})_{n \in [1, N]}$ verifying

$$n \in [1, N] \quad \vec{C}_k^{*(n)} = \mathcal{F}(\vec{C}_{k-1}^{*(n)}, \vec{e}_n) \quad (\text{A15})$$

where \vec{e}_n are the vectors of the canonical base of dimension N

$$\vec{e}_n = \begin{pmatrix} 0 \\ \vdots \\ 1 \\ 0 \\ \vdots \\ 0 \end{pmatrix} \leftarrow n\text{th position} \quad (\text{A16})$$

The asterisk denotes that the solutions $(\vec{C}_k^{*(n)})_{n \in [1, N]}$ considered at this stage are not physically relevant: they are only used for the algebraic determination of the matrix A . For every n , the column vectors \vec{j}_n^* , of which the components $j_k^{*(n)}$ are defined by

$$j_k^{*(n)} = \frac{2nFDc_{\text{Ox}}^*}{a\Delta X} (C_{M,k}^{*(n)} - C_{M-1,k}^{*(n)}) \quad (\text{A17})$$

are calculated. Using A13, we have the matricial relations

$$n \in [1, N] \quad \vec{j}_n^* = A \cdot \vec{e}_n \quad (\text{A18})$$

Because of the choice made for the \vec{e}_n , the vector \vec{j}_n^* actually represents the n th column of matrix A . One can show that the components of the vector \vec{j}_n^* are simply shifted with respect to those of the vector \vec{j}_{n-1}^* so that computation of eq A15 for $n = 1$ suffices to generate all of the elements of A . Consequently, A has the particular following trigonal form:

$$A = \begin{pmatrix} j_1^{*(1)} & 0 & 0 & \dots & 0 \\ j_2^{*(1)} & j_1^{*(1)} & 0 & & 0 \\ j_3^{*(1)} & j_2^{*(1)} & j_1^{*(1)} & \ddots & \vdots \\ \vdots & \vdots & \vdots & \ddots & 0 \\ j_N^{*(1)} & j_{N-1}^{*(1)} & j_{N-2}^{*(1)} & \dots & j_1^{*(1)} \end{pmatrix} \quad (\text{A19})$$

Discretization of the Poisson Equation: Computation of the Potential Distribution. Discretization of eqs 14–17 leads to

$$k \in [2, N-1] \quad V_{k-1} - 2V_k + V_{k+1} + \mu j_k = 0 \quad (\text{A20})$$

$$-V_1 + V_2 + V_{N-1} + V_N = 0 \quad (\text{A21})$$

$$V_1 - V_N - \Delta\varphi_s = 0 \quad (\text{A22})$$

μ being the constant given by

$$\mu = \frac{2L_0\Delta Y^2}{aK^L} \quad (\text{A23})$$

Using eq A13, we write the currents j_k

$$j_k = \sum_{p=1}^N a_{k,p} Q_p \quad (\text{A24})$$

$(a_{k,p})_{k \in [1, N], p \in [1, N]}$ being the components of matrix A as determined in the previous section (eq A19) and Q_k the functions of V_k defined by

$$Q_k = \frac{c_{\text{Ox}}^* + c_{\text{R}}^*}{c_{\text{Ox}}^*} \frac{\exp[-nf(V_k - V^0)]}{1 + \exp[-nf(V_k - V^0)]} - 1 \quad (\text{A25})$$

The nonlinear system consisting of the N equations A20–A25 has the potentials V_k as the only unknown variables. This system was solved using a Newton–Raphson-type method.²⁸ Once the V_k are known, the Q_k and j_k follow from eqs A25 and A24, respectively. The \vec{C}_k and the local concentration profiles are then calculated using eq A14. The ensuing bipolar current I_f was obtained by integrating the local faradaic currents by means of the trapezoid method.

Errors Inherent to the Discrete Analysis of the Problem.

The error made using the inverse Euler method applied to the convective diffusion equation (eqs A5–A7) is of the order $O(\Delta Y + \Delta X^2)$ and the one made in the finite difference scheme applied to the local electroneutrality equation (eqs A20–A25) is $O(\Delta Y^2)$.^{27,29} The computations were made with $M = 10^4$ iterations for the X direction and $N = 500$ – 10^3 iterations for the Y direction, which yields convergence of the results within a satisfactory computation time.

Glossary of Symbols

a	Gap of the thin-layer chamber
a_p	Particle radius
c_{Ox}	Local concentration of the Ox species
c_{Ox}^*	Bulk concentration of the Ox species
c_{R}	Local concentration of the R species
c_{R}^*	Bulk concentration of the R species
C_{Ox}	Dimensionless concentration difference for the Ox species
C_{R}	Dimensionless concentration difference for the R species
D_{Ox}	Diffusion coefficient for the Ox species
D_{R}	Diffusion coefficient for the R species
D	Diffusion coefficient $D = D_{\text{Ox}} = D_{\text{R}}$
E	Local electric field strength
E_0	Applied field in the solution
f	Defined by $F/(RT)$
f_{Ox}	Function of the position Y
F	Faraday number
I_f	Overall bipolar current
I_{Ω}	Overall ohmic current
j	Local current density
K^L	Conductivity of the electrolyte solution
l	Width of the metallic substrates
Superscript l	Pertaining to the diffusion limiting-current condition
L_0	Length of the metallic substrates
n	Number of electrons
Ox	Oxidized species
R	Reduced species
R	Gas constant
T	Temperature
v_{ef}	Electrophoretic velocity of a particle
v_Y	Velocity flow according to the Y -axis in the thin-layer channel
v^0	Characteristic velocity of the solution in the thin-layer channel
V	Local potential of the solution with respect to the equipotential metallic phase
V^N	Nernst potential
V^0	Standard potential for the redox couple Ox/R

V^*	Potential at $Y = Y_0$
x, y, z	Cartesian coordinates
X, Y, Z	Dimensionless Cartesian coordinates
Y_0	Position for which $j(Y=Y_0) = 0$
$\Delta\varphi_s$	Lateral applied potential difference
$\Delta\varphi^d$	Overpotential required for water electrolysis
$\Delta\varphi_{\text{str}}$	Streaming potential
ΔP	Tangential applied pressure drop
β	Coefficient in the power law $(\Delta P)^{1/\beta}$
γ	Fraction of the total overpotential that occurs on either side of a bipolar metallic particle
δ	Thickness of the diffusion layer
ϵ_0	Dielectric permittivity of vacuum
ϵ_r	Relative dielectric permittivity of water
ϕ	Ratio a/l
κ	Inverse of the Debye length
η	Dynamic viscosity
τ_C	Characteristic convection time
τ_D	Characteristic diffusion time
τ_M	Characteristic time at which the streaming potential measurements are performed
ζ	Electrokinetic potential (ζ -potential)

References and Notes

- (1) Longworth, L. G. In *Electrophoresis: Theory, Methods, and Applications*; Bier, M., Ed.; Academic Press: New York, 1959; Vol. II.
- (2) Lyklema, J. Solid-Liquid Interfaces. *Fundamentals of Interface and Colloid Science*; Academic Press: London, 1995; Vol. II, p 4.9.
- (3) Lyklema, J. Solid-Liquid Interfaces. *Fundamentals of Interface and Colloid Science*; Academic Press: London, 1995; p 4.54.
- (4) Von Helmholtz, H. *Ann. Phys.* **1879**, 7, 337.
- (5) Von Smoluchowski, M. *Bull. Int. Acad. Sci. Cracovie* **1903**, 184. Von Smoluchowski, M. In *Handbuch der Electricität und des Magnetismus*; Graetz, W., Ed.; Barth Leipzig: 1914; Vol. II, p 366. Von Smoluchowski, M. *Z. Phys. Chem.* **1918**, 92, 129.
- (6) Hückel, E. *Phys. Z.* **1924**, 25, 204.
- (7) Onsager, L. *Phys. Z.* **1926**, 27, 388.
- (8) Lyklema, J. The Role of Surface Conduction in the Development of Electrokinetics. In *Interfacial Electrokinetics and Electrophoresis*; Delgado, A. V. Ed.; Surfactant Science Series, Vol. 106; Marcel Dekker: New York, 2002; Chapter 3.
- (9) Hunter, R. J. *Zeta Potential in Colloid Science. Principles and Applications*; Academic Press: London, 1981.
- (10) Dukhin, S. S. *Adv. Colloid Interface Sci.* **1991**, 35, 173.
- (11) Baran, A. A.; Mishchuk, N. A.; Prieve, D. C. *J. Colloid Interface Sci.* **1998**, 207, 240.
- (12) Duval, J.; Huijs, G. K.; Threels, W. F.; Lyklema, J.; van Leeuwen, H. P. *J. Colloid Interface Sci.* **2003**, 260, 95.
- (13) Baran, A. A.; Babich, Y. A.; Tarovsky, A. A.; Mischuk, N. A. *Colloids Surf.* **1992**, 68, 141.
- (14) Duval, J.; Minor, M.; Cecilia, J.; van Leeuwen, H. P. *J. Phys. Chem. B* **2003**, 107 (17), 4143.
- (15) Keh, H. J.; Li, W. J. *J. Electrochem. Soc.* **1994**, 141 (11), 3103.
- (16) Yen, S.-C.; Yao, C.-Y. *J. Electrochem. Soc.* **1991**, 138 (9), 2697.
- (17) Fleischmann, M.; Ghoroghchian, J.; Pons, S. *J. Phys. Chem.* **1985**, 89, 5530.
- (18) Fleischmann, M.; Ghoroghchian, J.; Rolinson, D.; Pons, S. *J. Phys. Chem.* **1986**, 90, 6392.
- (19) Duval, J. *J. Colloid Interface Sci.*, submitted for publication.
- (20) Van Wagenen, R. A.; Andrade, J. D. *J. Colloid Interface Sci.* **1980**, 76 (2), 305.
- (21) White, F. M. *Fluid Mechanics*, second ed.; McGraw-Hill: New York, 1986.
- (22) Duval, J.; Kleijn, J. M.; van Leeuwen, H. P. *J. Electroanal. Chem.* **2001**, 505, 1.
- (23) Kaplan, W. *Advanced Calculus*, 2nd ed.; Addison-Wesley: Reading, MA, 1973.
- (24) Levich, V. G. *Physicochemical Hydrodynamics*; Prentice-Hall: Englewood Cliffs, NJ, 1962; p 114.
- (25) Leveque, M. A., *Ann. Mines. Mem. Ser.* **1928**, 12/13, 201.
- (26) Lyklema, J. Solid-Liquid Interfaces. *Fundamentals of Interface and Colloid Science*; Academic Press: London, 1995; Vol. II, p 4.27.
- (27) Ames, W. F. *Numerical Analysis of Partial Differential Equations*, third ed.; Academic Press: New York, 1992.
- (28) Press, W. H.; Teukolsky, S. A.; Vetterling, W. T.; Flannery, B. P. *Numerical Recipes in Fortran, The art of Scientific Computing*, 2nd ed.; Cambridge University Press: Cambridge, U.K., 1986.
- (29) Dautray, R.; Lions, J. L. In *Analyse Mathématique et Calcul Numérique pour les Sciences et les Techniques*; Evolution Numérique; Transport, Edition Masson: 1988; Vol. 9.